Supporting Information for

Exploring the Sensitivity of Lunar Interior Structure from Geophysical and Geochemical Constraints

H. Fuqua Haviland[1*], P. M. Bremner[1*], A. Mallik[2,3*], M. R. Diamond[4*], S. Panovska[5], S. J. Lock[6]

[1]Heliophysics and Planetary Science Branch, Marshall Space Flight Center.

[2]Bayerisches Geoinstitut, University of Bayreuth, Bayreuth, Germany.

[3]Department of Geosciences, University Arizona.

[4]Earth and Planetary Science Department, University of California, Berkeley.

[5]GFZ Helmholtz-Zentrum Potsdam.

[6]Division of Geological and Planetary Sciences, California Institute of Technology.

Corresponding author: Heidi Fuqua Haviland (heidi.haviland@nasa.gov)

**These authors contributed equally.*

Contents of this file

Additional Supporting Information (Files uploaded separately)

Supplemental Table S6: excel table with pMELTS composition

Description of supplemental materials

Provided below are a glossary of key terms, additional figures and tables as a supplement to those provided in the manuscript, and additional description of calculations. This includes the results from the full range of temperature profiles (MaxT, MeanT, MinT), and compositional model subclasses, compositionally homogeneous Hauri (CH-H), compositionally homogeneous Taylor (CH-T) and

compositionally stratified (CS). Model compositions are defined in Figure 1 and temperature profiles are defined in Figure 2 of the main text. Section S1 provides additional description of the ilmenite sinking calculations discussed in the main text. Table S7 is uploaded separately.

Glossary:

BC-RMSND: Bulk Chemistry RMSND
BurnMan: equation of state algorithm developed for Earth's lower mantle, v0.90 (Cottaar et al, 2014, 2016)
CH: Compositionally homogeneous
CH-H: Hauri compositional model, accounting for the removal of a 40 km GRAIL-era crust (Hauri et al., 2015)
CH-T: Taylor compositional model, accounting for the removal of a 70 km Apollo-era crust (S.R. Taylor, 1982)
CMB: Core-Mantle Boundary
Comb-RMSND: RMSND from combined GL2norm and BCl2norm
CS: Compositionally stratified
DE: Differential Evolution optimization algorithm (Price et al., 2005)
G-RMSND: composition model RMSND relative to mass and MOI
Ga: equivalent to Gyr meaning Billion Years ago
GRAIL: NASA's Gravity Recovery and Interior Laboratory mission
LMO: Lunar Magma Ocean
LRO: NASA's Lunar Reconnaissance Orbiter currently orbiting the Moon.
R_L : Standard Gravity Reference Lunar Radius, R_L = 1,738 km (*Williams et al.*, 2014)
MaxT: selenotherm based on upper bounds resulting from integrating (Gagnepain-Beyneix et al., 2006; Khan et al., 2006, 2007)
MeanT: selenotherm based on mean of MinT and MaxT.
MinT: selenotherm based on lower bounds from integrated profiles, same as MaxT.
Model class: a laterally averaged 1D compositional profile of the Moon (CH-H, CH-T, CS)
Model subclass: the pairing of a the 3 lunar temperature profiles with one of the 3 model classes (total of 9)
MO: Magma Ocean
MOI: Moment of Inertia, Table S3, (Williams et al., 2014)
Myr: Million years ago
R_{core} : Core Radius, ~400 km (Weber et al., 2011; Garcia et al., 2011, 2012; Hood et al., 1999)
R_{crust}: Thickness of Crust, 40km (Wieczorek et al., 2013, (average crustal thickness))
RMSND: Root Mean Square Normalized Deviation
Selenoman: equations of state algorithm developed herein for the Moon based on Burnman codes
Selenotherm: lunar temperature profile, akin to a geotherm of Earth
zscore: the number of standard deviations ($n\sigma$) of the model *value* from the reference (*ref*) values normalized by the measurement error (*stderr)* (equation 1)

Supplemental Tables

Table S1. Burnman inputs [mineral end member weight fractions] for each layer in the Compositionally Homogeneous Hauri (CH-H), Taylor (CH-T) and Compositionally Stratified (CS) Model Classes.

Homogeneous - Hauri (CH-H): Radius (km)	plg_an	sp_sp	sp_hc	ol_fo	ol_fa	opx_en	opx_fs	cpx_di	cpx_he	gt_py	gt_al	gt_gr	ilm	fe_fcc	fe_bcc
Inner Core	0.000	0.000	0.000	0.000	0.000	0.000	0.000	0.000	0.000	0.000	0.000	0.000	0.000	1.000	0.000
Outer Core	0.000	0.000	0.000	0.000	0.000	0.000	0.000	0.000	0.000	0.000	0.000	0.000	0.000	0.000	1.000
Lower Ilmenite	0.030	0.000	0.000	0.000	0.000	0.000	0.000	0.150	0.660	0.000	0.000	0.000	0.160	0.000	0.000
Lower Mantle	0.000	0.000	0.000	0.636	0.075	0.186	0.018	0.045	0.004	0.023	0.006	0.007	0.000	0.000	0.000
Mid Mantle	0.000	0.000	0.000	0.636	0.075	0.186	0.018	0.045	0.004	0.023	0.006	0.007	0.000	0.000	0.000
Upper Mantle	0.000	0.030	0.004	0.582	0.071	0.228	0.026	0.054	0.005	0.000	0.000	0.000	0.000	0.000	0.000
Upper Ilmenite	0.030	0.000	0.000	0.000	0.000	0.000	0.000	0.150	0.660	0.000	0.000	0.000	0.160	0.000	0.000
Crust	1.000	0.000	0.000	0.000	0.000	0.000	0.000	0.000	0.000	0.000	0.000	0.000	0.000	0.000	0.000

Homogeneous - Taylor (CH-T): Radius (km)	plg_an	sp_sp	sp_hc	ol_fo	ol_fa	opx_en	opx_fs	cpx_di	cpx_he	gt_py	gt_al	gt_gr	ilm	fe_fcc	fe_bcc
Inner Core	0.000	0.000	0.000	0.000	0.000	0.000	0.000	0.000	0.000	0.000	0.000	0.000	0.000	1.000	0.000
Outer Core	0.000	0.000	0.000	0.000	0.000	0.000	0.000	0.000	0.000	0.000	0.000	0.000	0.000	0.000	1.000
Lower Ilmenite	0.030	0.000	0.000	0.000	0.000	0.000	0.000	0.150	0.660	0.000	0.000	0.000	0.160	0.000	0.000
Lower Mantle	0.000	0.000	0.000	0.524	0.100	0.240	0.035	0.064	0.008	0.018	0.007	0.005	0.000	0.000	0.000
Mid Mantle	0.000	0.000	0.000	0.525	0.098	0.244	0.037	0.057	0.008	0.018	0.007	0.006	0.000	0.000	0.000
Upper Mantle	0.000	0.024	0.005	0.484	0.092	0.277	0.047	0.063	0.009	0.000	0.000	0.000	0.000	0.000	0.000
Upper Ilmenite	0.030	0.000	0.000	0.000	0.000	0.000	0.000	0.150	0.660	0.000	0.000	0.000	0.160	0.000	0.000
Crust	1.000	0.000	0.000	0.000	0.000	0.000	0.000	0.000	0.000	0.000	0.000	0.000	0.000	0.000	0.000

Stratigraphic Model (CS): Radius (km)	plg_an	sp_sp	sp_hc	ol_fo	ol_fa	opx_en	opx_fs	cpx_di	cpx_he	gt_py	gt_al	gt_gr	ilm	fe_fcc	fe_bcc
Inner Core	0.000	0.000	0.000	0.000	0.000	0.000	0.000	0.000	0.000	0.000	0.000	0.000	0.000	1.000	0.000
Outer Core	0.000	0.000	0.000	0.000	0.000	0.000	0.000	0.000	0.000	0.000	0.000	0.000	0.000	0.000	1.000
Lower Ilmenite	0.030	0.000	0.000	0.000	0.000	0.000	0.000	0.150	0.660	0.000	0.000	0.000	0.160	0.000	0.000
Lower Mantle	0.000	0.000	0.000	0.827	0.102	0.052	0.008	0.000	0.000	0.009	0.002	0.000	0.000	0.000	0.000
Mid Mantle	0.000	0.000	0.000	0.918	0.082	0.000	0.000	0.000	0.000	0.000	0.000	0.000	0.000	0.000	0.000
Upper Mantle 3	0.000	0.000	0.000	0.000	0.000	0.883	0.117	0.000	0.000	0.000	0.000	0.000	0.000	0.000	0.000
Upper Mantle 2	0.000	0.000	0.000	0.489	0.133	0.000	0.000	0.274	0.104	0.000	0.000	0.000	0.000	0.000	0.000
Upper Mantle 1	0.000	0.000	0.000	0.000	0.000	0.000	0.000	0.532	0.469	0.000	0.000	0.000	0.000	0.000	0.000
Upper Ilmenite	0.030	0.000	0.000	0.000	0.000	0.000	0.000	0.150	0.660	0.000	0.000	0.000	0.160	0.000	0.000
Crust	1.000	0.000	0.000	0.000	0.000	0.000	0.000	0.000	0.000	0.000	0.000	0.000	0.000	0.000	0.000

Mineral abbreviations: plg_an: plagioclase_anorthite; sp_sp: spinel_spinel; sp_hc: spinel_hercynite; ol_fo: olivine_forsterite; ol_fa: olivine_fayalite; opx_en: orthopyroxene_enstatite; opx_fs: orthopyroxene_ferrosilite; cpx_di: clinopyroxene_diopside; cpx_he: clinopyroxene_hedenbergite; gt_py: garnet_pyrope; gt_al: garnet_almandine; gt_gr: garnet_grossular; ilm: ilmenite; fe_fcc: iron_face-centered-cubic; fe_bcc: iron_body-centered-cubic.

Table S2. Published bulk silicate Moon compositions. All compositions are reported in weight percent. Final rows gives the unweighted average and standard deviations of the published compositions which were used to compare to the models calculated in this work.

SiO_2	TiO_2	Al_2O_3	FeO	MgO	CaO	Sum	Reference
45.90	0.30	6.00	10.50	32.40	4.90	100	Taylor and Bence (1975), Taylor (1980) (CI value of Mg/Si assumed)
45.84	0.20	4.61	13.07	32.47	3.81	100	Wanke et al. (1977) (CI value of Mg/Si assumed)
44.98	0.30	4.22	13.96	32.83	3.71	100	Ringwood (1977)
43.52	0.39	7.62	13.07	29.25	6.16	100	Morgan et al. (1978) (model 4B, CI value of Mg/Si assumed)
44.98	0.30	4.22	13.96	32.83	3.71	100	Ringwood (1979)
48.63	0.40	5.02	12.96	29.14	3.85	100	Buck and Toksoz (1980)
44.50	0.18	3.78	12.71	35.66	3.16	100	Wanke and Dreibus (1982)
44.79	0.31	6.19	11.04	33.02	4.64	100	Taylor (1982)
41.70	0.19	4.16	10.32	40.30	3.33	100	Delano and Lindsey (1983)
42.52	0.19	3.69	13.57	37.03	2.99	100	Jones and Delano (1989)
45.90	-	4.60	13.10	32.60	3.80	100	Wanke and Dreibus (1986)
43.47	0.30	3.74	12.32	37.13	3.05	100	Ringwood et al. (1987)
44.83	0.19	3.92	12.46	35.28	3.32	100	O'Neill (1991)
49.90	-	6.90	10.80	27.50	4.90	100	Kuskov (1997)
50.00	-	6.30	10.40	28.50	4.80	100	Kuskov and Kronrod (1998) Model I
48.50	-	5.90	11.70	29.60	4.30	100	Kuskov and Kronrod (1998) Model II
43.75	0.30	6.05	13.10	32.26	4.54	100	Taylor (1999)
47.17	0.18	3.90	9.31	36.35	3.08	100	Warren (2005) (Mg/Si = 1.1*CI)
47.20	0.18	3.90	9.32	36.31	3.09	100	Warren (2005) (Mg/Si = 1.1*CI, excluding 1.2 wt.% core)
47.42	0.17	3.63	9.37	36.53	2.88	100	Warren (2005) (Th = 65 ppb)
48.72	0.18	3.90	9.00	35.11	3.09	100	Warren (2005) (Mg/Si = 1.03*CI)
45.69	0.18	3.90	9.61	37.52	3.09	100	Warren (2005) (Mg/Si = 1.17*CI)

47.73	0.18	3.91	8.36	36.73	3.09	100	Warren (2005) (MgO/FeO = 4.4)
46.50	0.18	3.90	10.53	35.80	3.09	100	Warren (2005) (MgO/FeO = 3.4)
48.64	0.17	3.62	10.70	34.01	2.87	100	Warren and Dauphas (2014)
45.43	0.20	4.49	8.13	38.16	3.58	100	Hauri et al. (2015)
46.09	**0.24**	**4.70**	**11.28**	**34.01**	**3.72**	**100**	**Average**
2.21	**0.07**	**1.16**	**1.80**	**3.31**	**0.83**		**Standard Deviation (1σ)**

Table S3. Values of observed lunar mass and normalized moment of inertia used to determine model misfit (Williams et al., 2014). The average of the published bulk silicate Moon compositions along with the 1σ standard deviation show in Table S2.

(A)	**Mass**	**MOI**	**Radius**
Value	7.34630e22 kg	0.392728	1,738 km
Standard Error	0.00088e22 kg	0.000012	

(B)	**SiO_2**	**TiO_2**	**Al_2O_3**	**FeO**	**MgO**	**CaO**
Average (weight %)	46.09	0.24	4.70	11.28	34.01	3.72
Standard dev (weight %)	2.21	0.07	1.16	1.80	3.31	0.83

Table S4. ASPECT Model parameters.

Parameters	**Value**
Thickness of the ilmenite-rich layer	30 km
Inner radius of 2D spherical shell	330 km
Outer radius of 2D spherical shell	1,670 km
Mantle density	3,400 kg m^{-3} [a]
Surface gravity acceleration	1.62 ms^{-2}
Mantle thermal expansion coefficient	2E-5 K^{-1}
Mantle thermal conductivity	3.0 W m^{-1} K^{-1}
Mantle specific heat capacity	1,000 J kg^{-1} K^{-1}
Surface temperature	250 K
Reference temperature	1,600 K [a]
Mantle viscosity	1.0^{21} Pa s[a]
Thermal viscosity exponent	9.0
Ilmenite-rich layer density	3,790 kg m^{-3}
Composition viscosity prefactor	1E-3
Radiogenic heating rate	8.4927E-12 W/kg

[a](*Laneuville et al.*, 2014)

Table S5. Full Summary of layer thickness constraints.

Summary of layer thickness constraints under 2σ (G, BC) and 3σ (Combined, 3σ to include sufficient population size) for all model subclasses. Thickness ranges (Δd, *km*) and volumes (*km*^{3}) are tabulated and compared with the original ranges tested in Table 1 for the best fitting models. The reduced normalized range is 1 minus the normalized difference between the best fit Δd ranges and the maximum extent of the original. Since the reduced normalized ranges are relative to the same initial values, they indicate which *RMSND* values provide the best constraints of individual layers. More reduction from the initial range equals a lower % value. Model counts can be found in supplemental text S2.

Layer Name	***G-RMSND* Range Δd (*km*)**	**Reduced Normalized Range (%)**	***BC-RMSND* Range Δd (*km*)**	**Reduced Normalized Range (%)**	***Comb-RMSND* Range Δd (*km*)**	**Reduced Normalized Range (%)**
Inner Core	0 – 320	53%	0 – 598	100%	8 – 341	56%
Outer Core	43 – 338	49%	0 – 512	85%	1 – 338	56%
Lower Ilmenite	1 – 489	98%	0 – 480	96%	2 – 308	61%
Lower Mantle	13 – 974	57%	0 – 1,435	85%	15 – 999	58%
Mid Mantle	0 – 1,002	59%	0 – 1,391	82%	4 – 923	54%
Upper Mantle (CS:1,2,3)	0 – 883	52%	0 – 1,391	82%	0 – 863	51%
Upper Ilmenite	1 – 57	3%	0 – 25	1%	2 – 24	1%
Total Core	**234 – 401**	**14%**	**0 – 874**	**73%**	**269 – 387**	**10%**
Total Mantle	**926 – 1,352**	**25%**	**788 – 1,691**	**53%**	**1,093 – 1,352**	**15%**
	vol. (*km*^{3})		**vol. (*km*^{3})**		**vol. (*km*^{3})**	
Lower Ilmenite Volume	0 – 1.6e9	12%	0 – 8.8e8	7%	0 – 7.7e8	6%
Upper Ilmenite Volume	0 – 2.0e9	22%	0 – 8.9e8	4%	0 – 8.5e8	4%
Total Ilmenite Volume	**1.5e8 – 2.9e9**	**13%**	**2.2e8 – 9.0e8**	**3%**	**1.5e8 – 1.0e9**	**4%**

See Text S1 for Table S6.

Table S7 is uploaded separately

Supplemental Figures

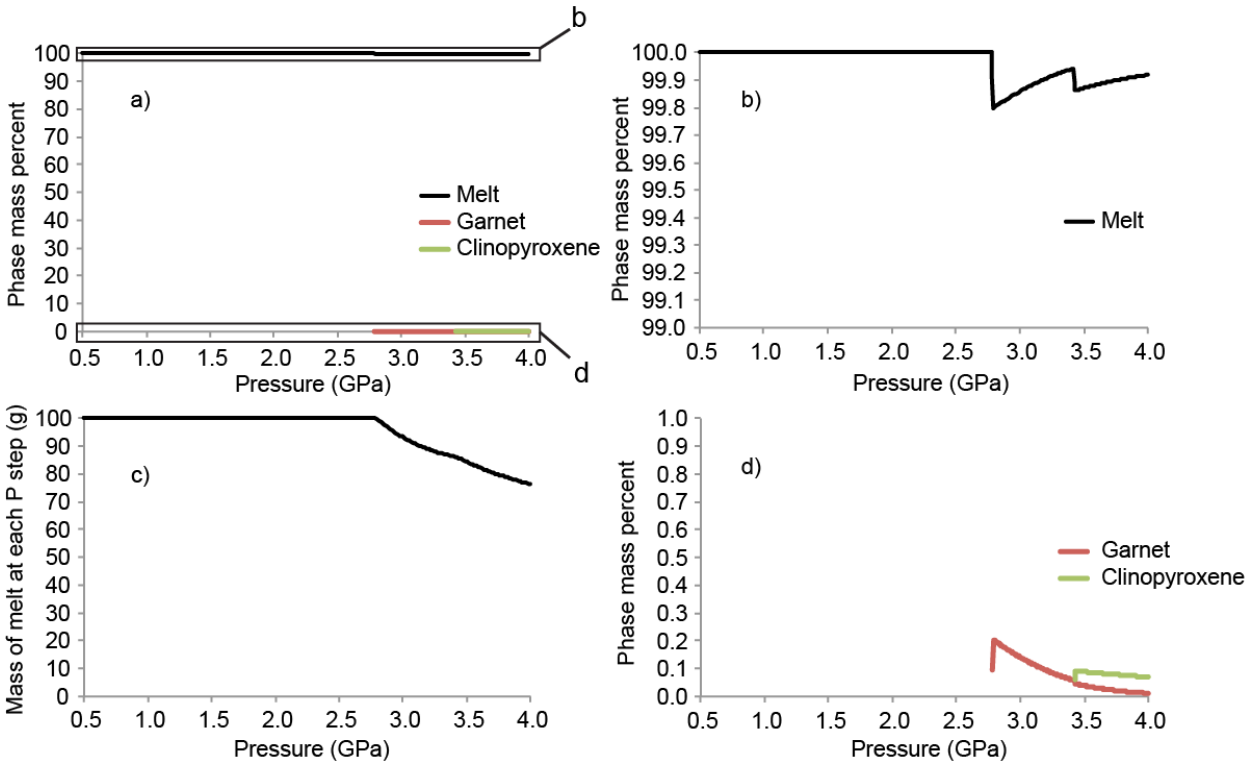

Figure S1. Mass of phases at each pressure step during sinking of Ti-rich partial melt through the lunar mantle at 1450 °C, without assimilating the surrounding mantle. The process is buffered at IW. a) Melt, garnet and clinopyroxene masses at each pressure. b) Magnification of box labeled 'b' in sub-panel a). c) Mass of melt at each pressure step. The mass of melt decreases deeper than 2.5 GPa due to saturation of garnet and/or clinopyroxene at the liquidus. d) Magnification of the box labeled 'd' in sub-panel a). The mass of phases at 1250 °C and 1350 °C as well as the composition of all the phases are available upon request to the corresponding author.

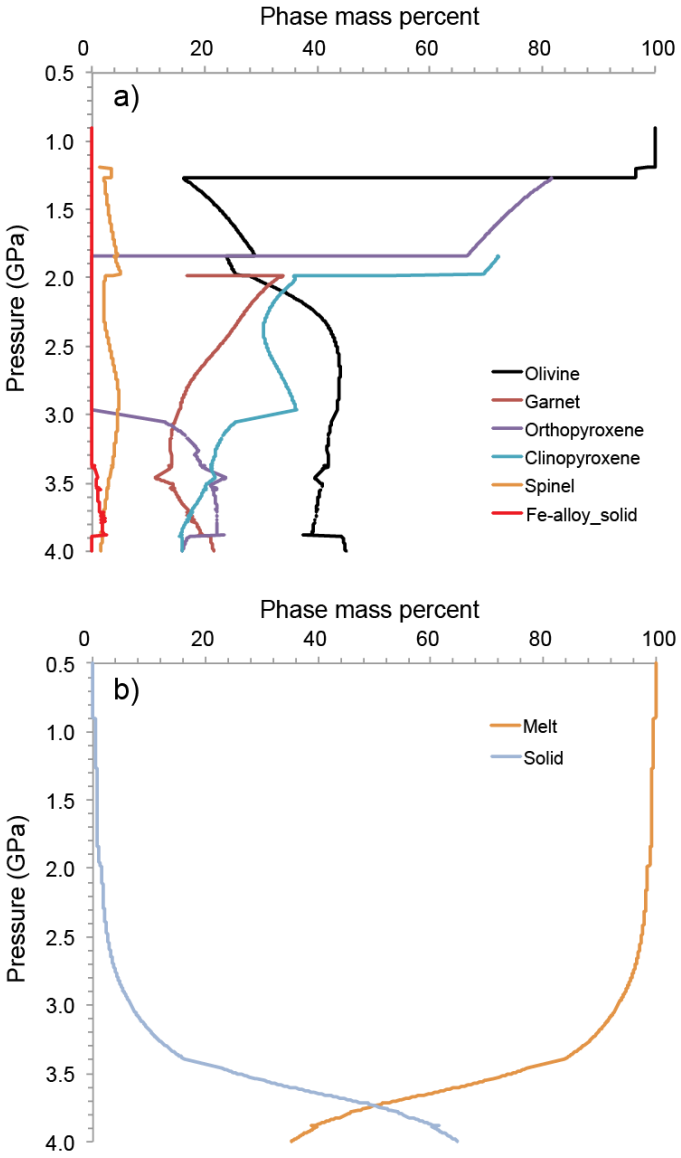

Figure S2. Percentage of mass of phases at each pressure step for assimilation of 2 g of mantle buffered at IW, for isothermal sinking of Ti-rich melt through the lunar mantle at 1450 °C. a) Mass percent of solid phases b) Mass percent of melt versus total solid phases. The solid phases formed at each pressure step are fractionated, and the residual melt after fractionation makes its way to the next pressure step where it is assimilated by 2 g of lunar mantle. Around 1 GPa, the residual melt enters sub-liquidus field by crystallizing olivine at its liquidus. The phase equilibria due to assimilation of 50 and 100 grams of the mantle, as well as the composition of all the phases will be available upon request to the corresponding author.

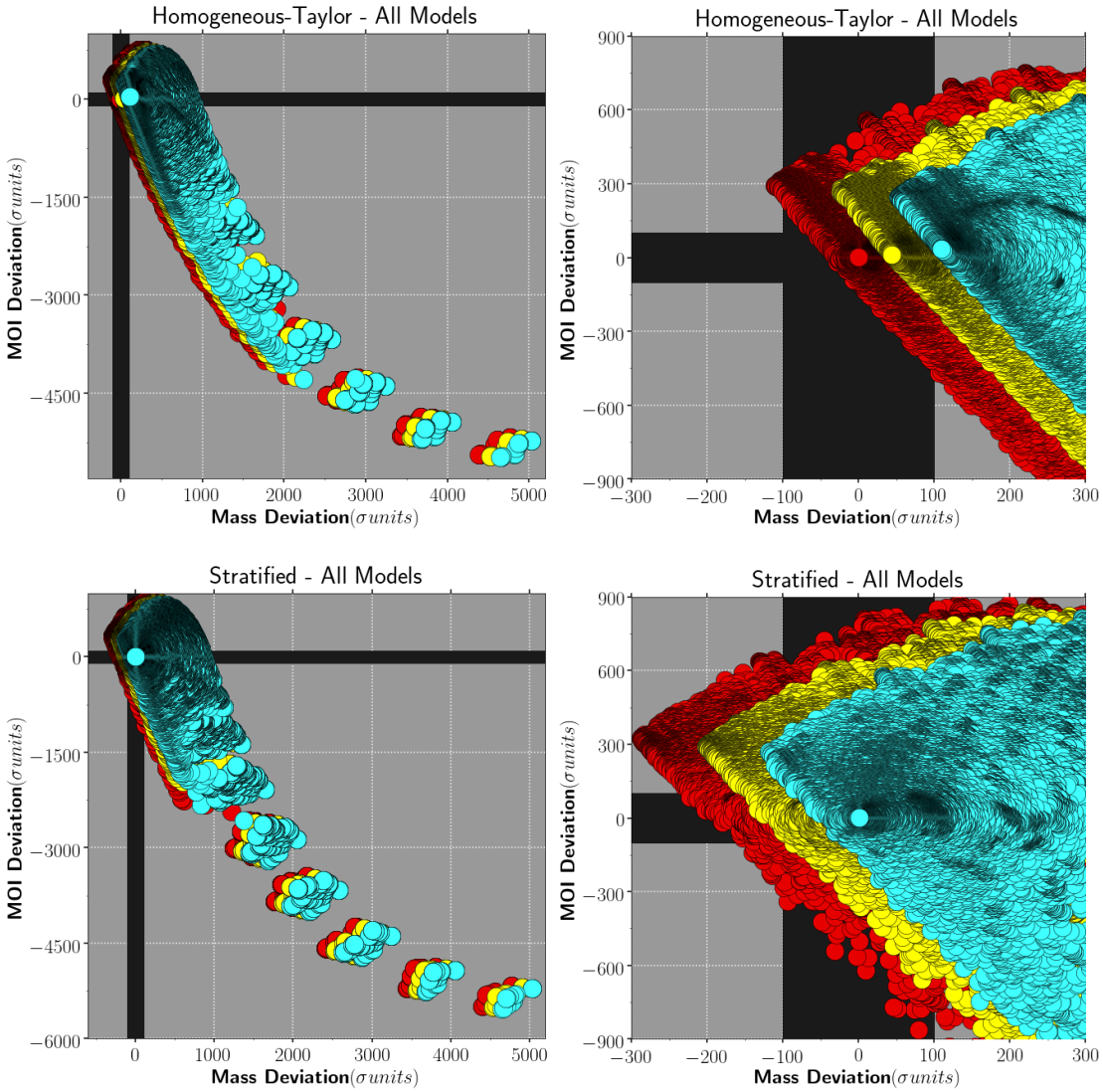

Figure S3. The influence of temperature is shown for the three subclasses for the CH-T (top panels) and CS (bottom panels) model classes for all models (left panels) and a zoomed window (right panels) as a function of the number of standard deviation misfits from observational Mass and MOI. Similar to Figure 3 (b), a systematic shift is visible where decreased model temperature corresponds to increased model mass, and is due to material densification with decreasing temperature. MaxT (red), MeanT (yellow), and MinT (cyan).

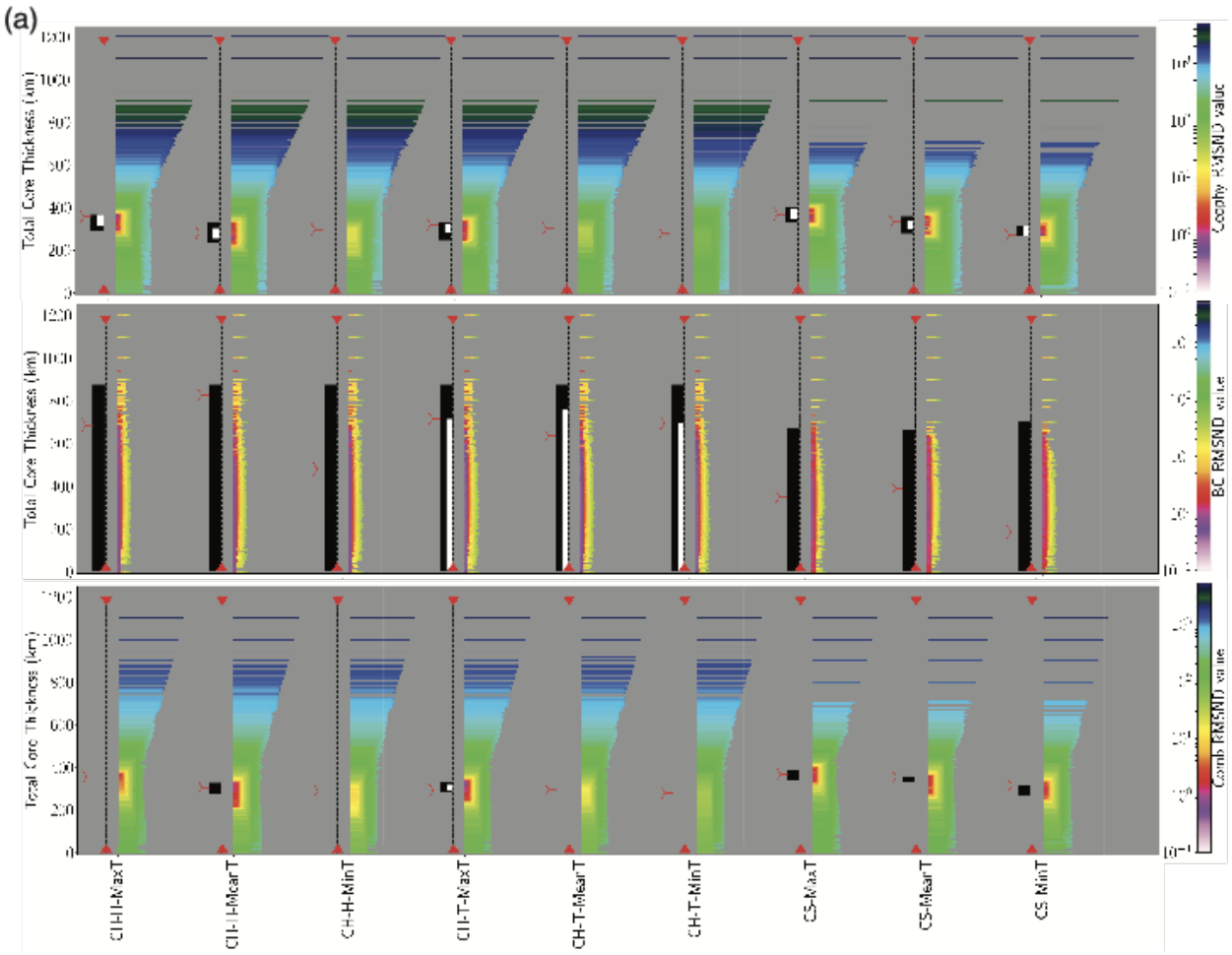
(a)
Total Core Thickness (km)
Total Core Thickness (km)
Total Core Thickness (km)
CH-H-MaxT
CH-H-MeanT
CH-H-MinT
CH-T-MaxT
CH-T-MeanT
CH-T-MinT
CS-MaxT
CS-MeanT
CS MinT

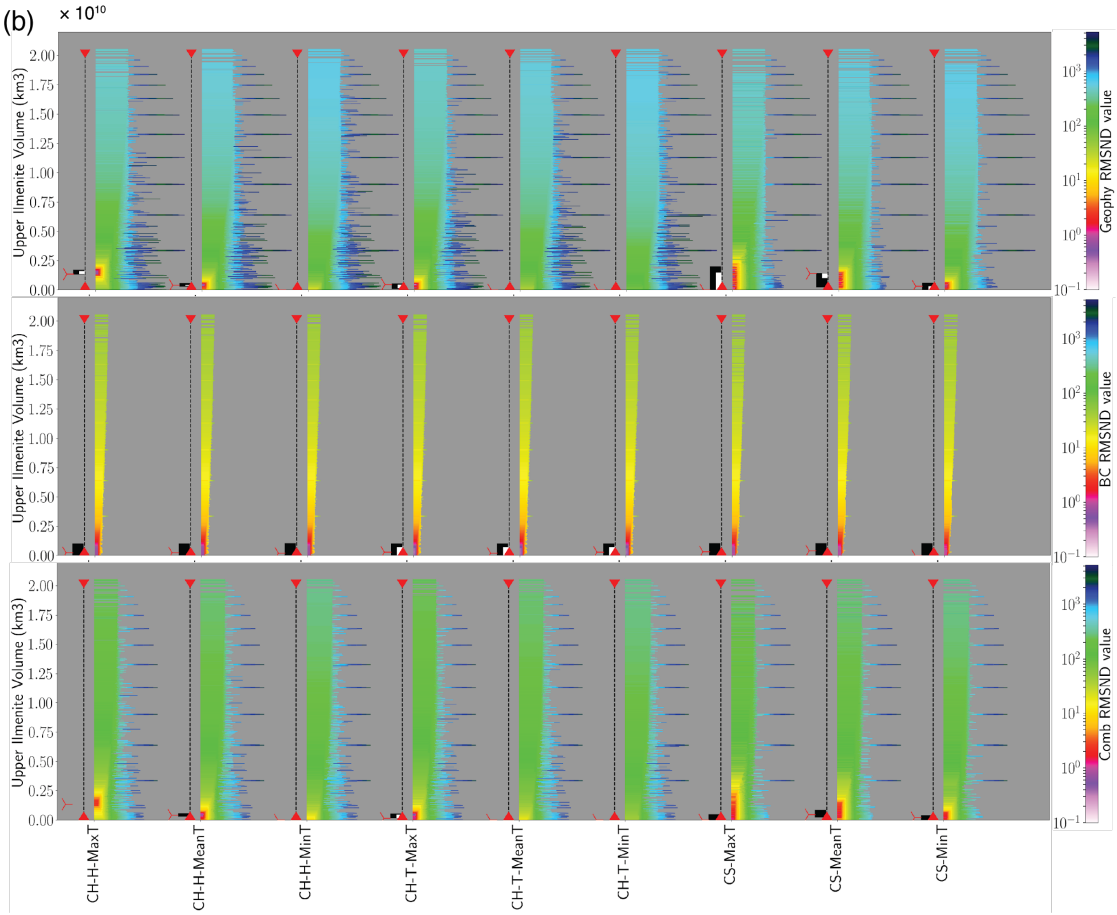
(b)
× 10^10
Upper Ilmenite Volume (km3)
2.00
1.75
1.50
1.25
1.00
0.75
0.50
0.25
0.00
Geophy RMSND value
BC RMSND value
Comb RMSND value
CH-H-MaxT
CH-H-MeanT
CH-H-MinT
CH-T-MaxT
CH-T-MeanT
CH-T-MinT
CS-MaxT
CS-MeanT
CS-MinT

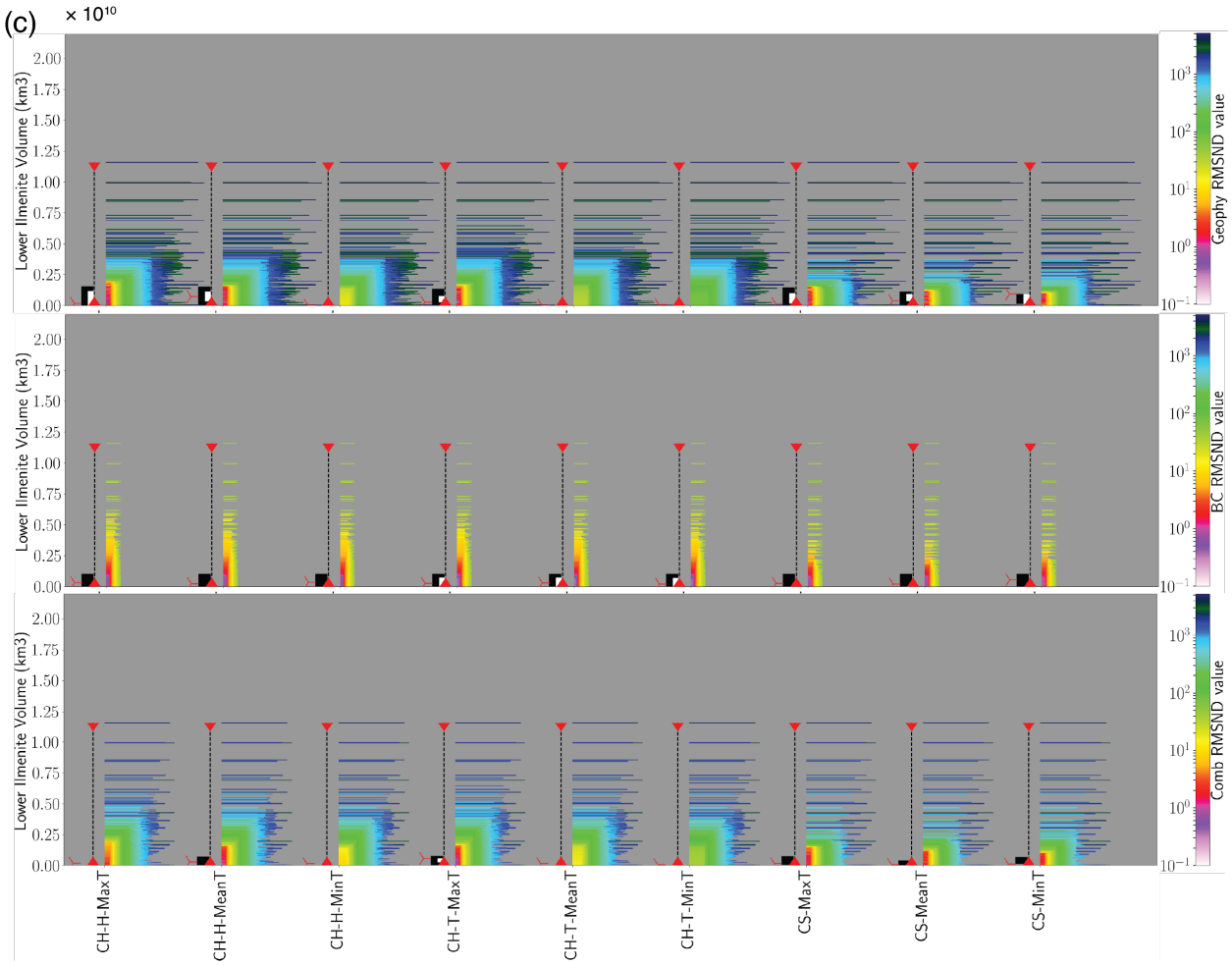
(c)
× 10¹⁰
Lower Ilmenite Volume (km3)
2.00
1.75
1.50
1.25
1.00
0.75
0.50
0.25
0.00
Geophy RMSND value
BC RMSND value
Comb RMSND value
CH-H-MaxT
CH-H-MeanT
CH-H-MinT
CH-T-MaxT
CH-T-MeanT
CH-T-MinT
CS-MaxT
CS-MeanT
CS-MinT

Figure S4 (d): Total Ilmenite Volume

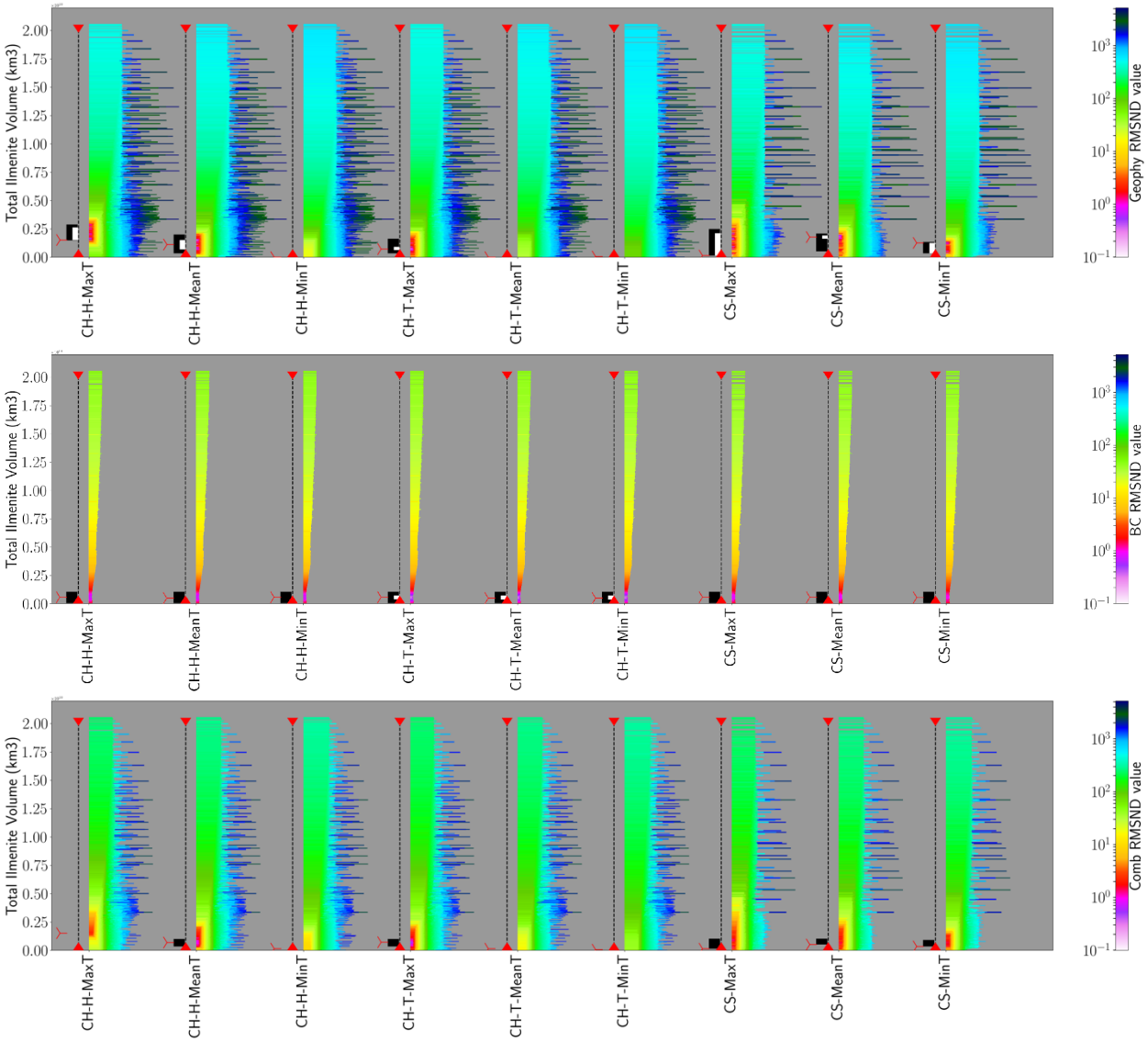

Figure S4. Enhanced box-and-whisker plots of the Total Core thickness (a), upper ilmenite-rich layer volume (b), and lower ilmenite-rich layer volume (c), and Total Ilmenite Volume (d), for all model subclasses (as labeled on x-axis). Each sampled lunar candidate model plots as a left-justified line where the length and color are vary according to the model's G-RMSND (top panels), BC-RMSND (middle panels), and Comb-RMSND value (bottom panels). High RMSND values correspond to the longer horizontal lines, and low RMSND values to short lines. Low RMSND values are plotted on top of larger values. To the left of each column of scaled lines are the "simplified" ranges where the min/max sampled layer thickness (or volume) is shown by red triangles and connected by a black dotted line. The black and white boxes indicate that all components within the RMSND value are less than or equal to 1σ and 3σ (1 or 3 zscores) misfit, respectively. The best fit thickness (or volume) is

marked with a red arrow tail for each model subclass. For additional Box and Whisker plots, see Figure 7.

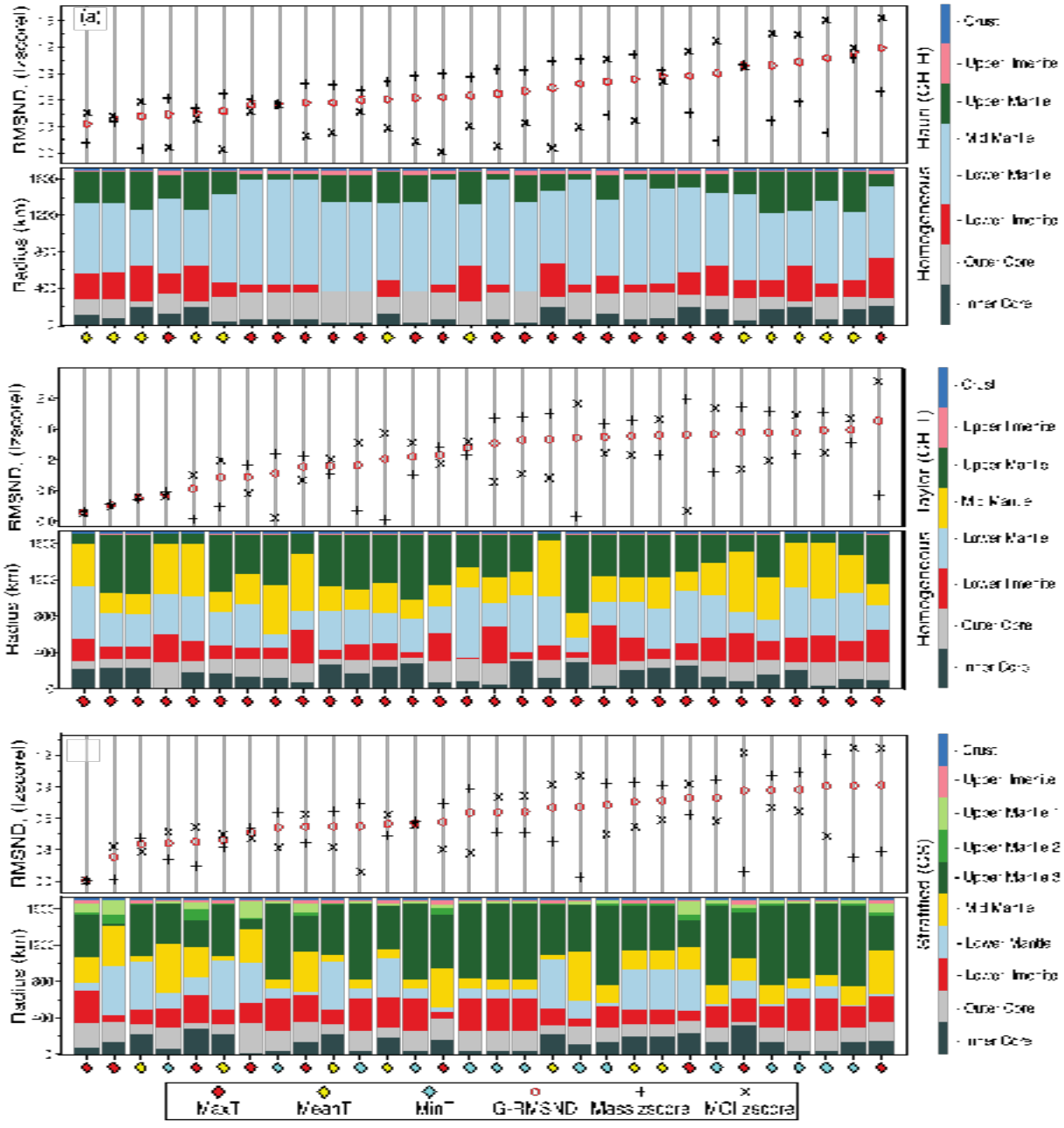

Figure S5. The top thirty best-fit models for (a) CH-H, (b) CH-T, and (c) CS model classes are compared in terms of deviations for Mass, MOI, and RMSND (top panel); and model stratigraphic structure with color coded layers (bottom panel). The stratigraphic legend is to the right of each set of panels. Diamonds along the x-axis indicate model temperature profile. Models are ordered by lowest G-RMSND. For compositional description of each layer, see Figure 1.

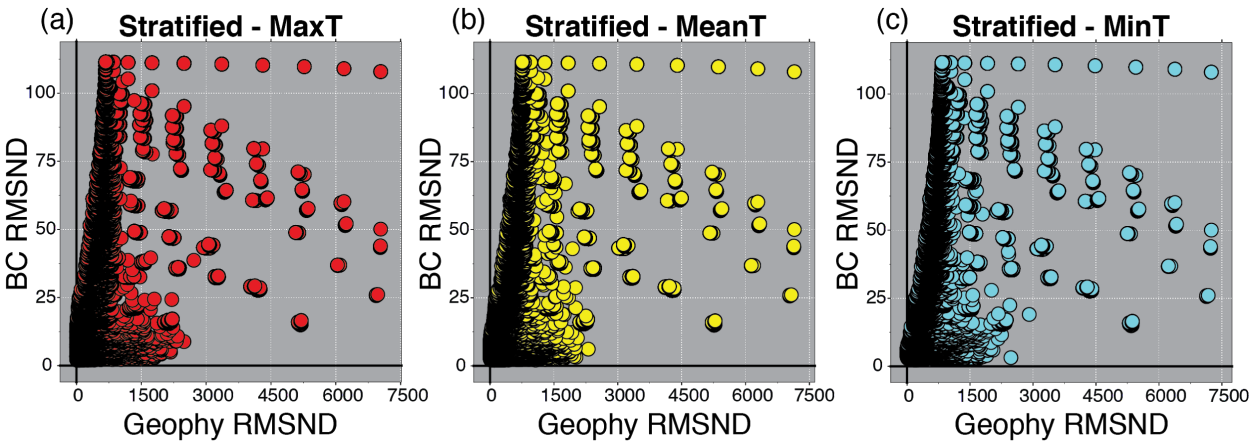

Figure S6. CS model class bulk chemistry RMSND compared to geophysical RMSND. Each circle represents a sampled lunar model candidate, and is colored according to thermal profile. For a given BC-RMSND value, sampled models span a wide range of G-RMSND values. However, the lowest G-RMSND values only correspond to low BC-RMSND values. Nearly equivalent distributions were observed for the CH-H and CH-T model classes.

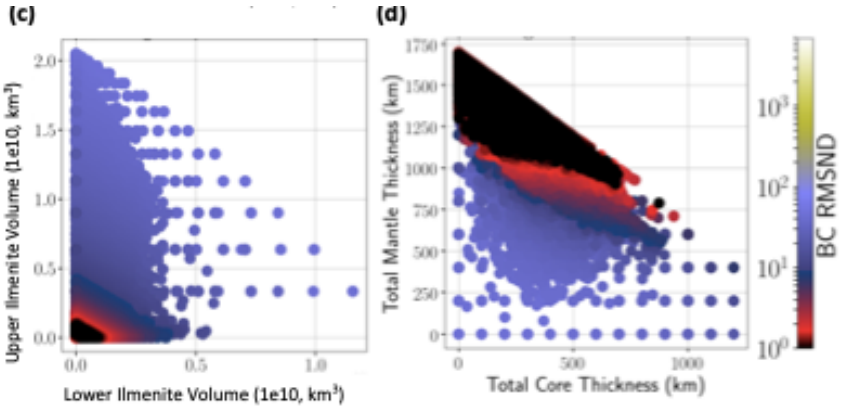

Figure S7. Layer trends are plotted for BC-RMSND values, see Figure 5e,f for G-RMSND results. The difference in patterns of the low RMSND values suggests that Mass and MOI provide better constraints of the Total Core size, but that the volume of ilmenite is better constrained with bulk composition.

See Text S1 for Figures S8, S9, S10, and S11.

Text S1. The sinking mechanism of an ilmenite-rich layer to the CMB as a partial melt

We found that an ilmenite-rich layer at the CMB today is consistent with, although not required by, the geochemical and geophysical constraints we applied. Additionally, we found that large volumes of ilmenite-rich material just beneath crust (upper ilmenite layer) penalize a model's fit to MOI and bulk chemistry constraints. Therefore, if a subcrustal ilmenite-rich layer existed post-LMO crystallization, then a significant fraction of the layer must have sunk into or through the mantle via some transport mechanism and remain stable over the lifetime of the Moon. However, we also observed that most of our best-fit models retained a small, but finite, volume of ilmenite just below the crust.

Here we explore the viability of potential mechanisms to transport ilmenite-rich material from the upper mantle of the early post-LMO crystallization to the CMB and whether it was possible to simultaneously retain a volume of ilmenite in the shallow mantle. We considered the early Moon in terms of composition and temperature profile and tested two end member cases: that ilmenite sinks as a melt, or as a solid. We begin with reviewing the proposed overturn processes (Section 1.1) Next, we present calculations of the density of melt of an ilmenite-rich layer at different depths in the mantle and consider the effect of possible assimilation of mantle material on the ability of ilmenite-rich partial melt to percolate to depth in the lunar mantle.We then assess the sinking and stability of this ilmenite-rich layer during mantle overturn and solid-state convection (Section S1.2) and draw conclusions (S1.3).

Text S1.1 Background: A review of Mantle Overturn Processes

Given that this study is motivated by the search for fingerprints of the overturn process in the present-day Moon, here we explore the details of LMO crystallization and overturn mechanisms, and their implications for a lunar dynamo. Pristine high-Ti ultramafic glasses acquired during the Apollo missions (Delano, 1986) imply Ti-enrichment within the lunar mantle. Phase equilibria experiments indicate that the high-Ti glasses found in basaltic lavas on the surface of the Moon are in equilibrium with a mantle assemblage as deep as 250 – 500 km (Delano, 1980; Green et al., 1975; Wagner & Grove, 1997). Such a deep source requires a mechanism which enrich portions of the lunar mantle in Ti. The most titaniferous layer formed during LMO fractional crystallization is an ilmenite-rich layer crystallized from the remnant liquid at a depth of ~100 km from the lunar surface, after ~95% crystallization of the LMO

(Elardo et al., 2011; Elkins Tanton et al., 2002; Snyder et al., 1992). Such an ilmenite-rich layer, estimated to be about 16% ilmenite and 84% clinopyroxene (Snyder et al., 1992), would have a density of 3.8 g/cm^3 as a solid, ~0.4-0.5 g/cm^3 denser than the underlying olivine+orthopyroxene-bearing mantle. Therefore, one mechanism for the sinking of an ilmenite-rich layer through the underlying mantle is solid-state advection driven by this density contrast. This would allow a shallow Ti-rich layer to sink to the deep mantle where it could later erupt to the surface as high-Ti lavas (Herbert, 1980; Hess & Parmentier, 1995; Ringwood & Kesson, 1976; de Vries et al., 2010). Alternatively, Elkins-Tanton et al. (2002) suggested that the high viscosity of this layer would prevent sinking as a solid. They suggested that the layer must have been partially molten and percolated through the underlying mantle. The layer could overturn while still in the partially molten state at the end of LMO crystallization (a possibility examined by Boukaré et al. (2018)) or could be heated by impact or radiogenic heating after MO solidification, resulting in partial melting and sinking of the partial melt through the underlying mantle (Elkins Tanton et al., 2002). Open questions still remain. The global extent of the LMO (Khan et al., 2014; Charlier et al., 2018, and references therein), the overturn sequence in terms of local small-scale or global large-scale transport mechanisms and the feasibility of such a mechanism for transporting ilmenite to the CMB is still unresolved (Borg et al., 2011; Dygert et al., 2016; Elkins Tanton et al., 2002; Li et al., 2019; Yu et al., 2019; Zhao et al., 2019).

Once a high-density (potentially partial-melt) layer has been produced at the CMB, the question arises as to its stability. Some studies suggest a partial melt layer would have a higher density than the surrounding mantle and so be stable at the CMB (Khan et al., 2014; Weber et al., 2011). Additionally, de Vries et al. (2010) showed ilmenite-rich cumulates can sink through the mantle and survive at the CMB during mantle convection using geodynamic simulations. They demonstrate this through analyzing a 2D convection model varying the density and internal heat production of the ilmenite-rich layer over 4.5 Ga. Recently, Mallik et al. (2019) evaluated the consequence of two possible scenarios: if the deep mantle partial melt is denser than the overlying mantle, the thermal state can be used to constrain the temperatures at the CMB; else, the partial melt could ascend reactively through the overlying mantle and contribute to the formation of mare basalts.

Text S1.1.1 Methods: Melt Calculations for an Early Moon

We test the hypothesis that a partial melt of an ilmenite-rich layer could sink to the CMB by percolation through the underlying mantle. We estimated the density of a partial melt composition of an ilmenite-rich layer as the melt sinks, using the Gibbs free energy minimization algorithm pMELTS (Ghiorso et al., 2002). We assumed that the melt sinks isothermally from 0.5 – 4 GPa (close to the pressure of CMB) across a range of lunar mantle temperatures from 1,200 – 1,450 °C. We allowed a fixed mass of mantle to be hybridized and assimilated by the melt as it sinks by porous reactive flow, as suggested by (Elkins Tanton et al., 2002), to capture two end member scenarios: (i) without the assimilation of the surrounding mantle, and (ii) continuously assimilating the surrounding mantle, maintaining equilibrium with the surrounding solid.

We chose the most Fe+Ti-rich partial melt composition of a modeled high-Ti cumulate composition (Van Orman & Grove, 2000) as our starting melt to equilibrate with our pMELTS modeled lunar mantle composition (Taylor, 1982) (see Table S6). We chose the most Fe+Ti-rich melt composition to estimate the maximum density contrast with the mantle and so place an upper limit on the ability of the melt to sink.

To validate the density of the titanium-rich melts calculated by pMELTS, we compared the densities of Apollo 14 black glass estimated by X-ray absorption (Sakamaki et al., 2010) and sink-float methods (Circone & Agee, 1996; Vander Kaaden et al., 2015) to the density of black glass estimated by pMELTS under the same range of pressure-temperature conditions (0.5 - 4 GPa, 1427 °C, 1430 °C, and 1827 °C; Figure S8 and S9). At 1427 °C, the densities from X-ray absorption, the sink-float method, and pMELTS, are nearly parallel to 2 GPa, at which point a kink in the calculated density curve develops due to the black glass crossing the liquidus at this depth. Such sub-liquidus conditions at ~2 GPa and 1427 °C are consistent with experimental phase equilibria of Apollo 14 black glass (Wagner & Grove, 1997). In contrast, the density as a function of depth of Sakamaki et al. (2010) at 1427 °C does not predict sub-liquidus conditions because density was measured by them at 1.19 GPa only and extrapolated to higher pressures using a Birch-Murnaghan equation of state. The density parameterization of Vander Kaaden et al. (2015) is based on sink-float experiments of Circone and Agee (1996) which were performed at temperatures higher than 1427 °C and at pressures greater than 1.5 GPa. This parameterization also linearly extrapolates for conditions above 1.5 GPa. The density of black glass estimated by

pMELTS agrees and lies within the density estimates of Vander Kaaden et al. (2015) and Sakamaki et al. (2010).

To simulate an open-system assimilation process, we used the fractional crystallization function in pMELTS to calculate the phase equilibria and densities of the melt and mantle from 0.5 – 4 GPa, at pressure steps of 0.005 GPa. While the mass of mantle assimilated at each pressure step was held constant within a run, the mass of mantle was varied across runs to test the effect of melt density on extent of mantle assimilation. The starting condition of the calculations was the Fe+Ti-rich partial melt at 0.5 GPa and fO_2 buffered at the iron to wüstite transformation (IW; within the range of oxygen fugacity conditions estimated for the lunar interior (Herd, 2008)). As the melt sank, it was equilibrated with 0 g, 2 g, 50 g, and 100 g of mantle mass (Figures S10) at each pressure step. When solid phases crystallized due to assimilation of mantle, the solids were fractionated *in-situ* such that only the residual melt proceeds to subsequent pressure steps, evolving the composition of the residual melt with depth. Three different calculations were run along mantle temperatures of 1250 °C, 1350 °C, and 1450 °C, see Figure S9.

Text S1.1.2. Results: Melt Calculations for an Early Moon

We find a crossover point between the density of modeled lunar mantle and the density of the melt at depth (Figure S10). Above the crossover, the melt is less dense than the mantle; thus, is positively buoyant. Below the crossover point, with increasing depth the melt becomes denser than the surrounding mantle, therefore, is negatively buoyant. This crossover depth occurs at ~180 km for the end member scenario of no mantle assimilation. Mantle assimilation increases the depth of the crossover, and with 50 g of mantle assimilation no crossover occurs and the melt remains positively buoyant over the depth range of our calculations. Therefore, in order for the ilmenite-bearing layer to percolate to depth as a melt, a mechanism is needed to transport the melt to depths below the crossover.

Can Fe+Ti-rich melt sink through the lunar mantle if it does not assimilate the surrounding mantle? Independent of temperature, the Fe+Ti-rich melt (without assimilating the mantle) is less dense than the surrounding mantle at shallow depths and is negatively buoyant relative to the lunar mantle between pressures of 1.6 - 1.8 GPa, or a depth of ~200 km (Figure S10). Therefore, an Fe+Ti-rich melt can sink through the lunar mantle due to negative buoyancy, possibly

accumulating at the base of the mantle. A major impact, such as during those during the Late Heavy Bombardment, can create a partially molten zone through sinking of Fe+Ti-rich melt as deep as 180-200 km (Morrison, 1998). This event would enable the Fe+Ti-rich partial melt of the ilmenite-rich layer to overcome the depth of the density barrier, after which it would sink to the CMB without impedance. Percolation may pose a limitation at low melt fractions.

Can Fe+Ti-rich melt sink through the lunar mantle if it does assimilate the surrounding mantle? With increasing proportion of mantle assimilation, the density of the residual melt initially sharply decreases with pressure, below which the melt density increases with depth (Figure S10a). This initial density decrease of the residual melt results from the dissolution of the assimilating mantle in the melt (causing a decrease in the TiO_2 and an increase in the Mg# of the melt composition; see Figure S10b and S10c and Table S6) because the condition is super-liquidus for the bulk composition of the Fe+Ti-rich melt and the assimilated mantle. The density decrease due to assimilation extends to 1.2 GPa (~200 km depth). At greater pressures, the melt density increases due to a combination of fractionation of mineral phases with depth (Figure S10) and the compressibility of the residual melt with increasing pressure. In the case of the lowest amount of mantle assimilation considered (2 *wt%* of mantle), the melt becomes negatively buoyant at 2.5 GPa, equivalent to a depth of 500 km. To our knowledge, no process can explain a mechanism to force the Fe+Ti-rich melt to reach such a deep density barrier. With 50-100 *wt%* of mantle assimilation, the residual melt is positively buoyant relative to the mantle at all pressures, implying that such a residual melt would never sink through the mantle. Thus, significant mantle assimilation in a Fe+Ti-rich melt inhibits the sinking of melt through the lunar mantle.

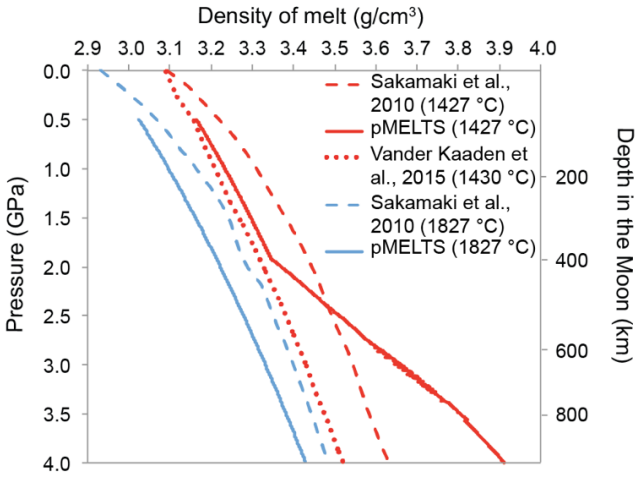

Figure S8. Density profiles of Apollo 14 black glass estimated by X-ray absorption technique (*Sakamaki et al.*, 2010) compared to density profiles of the high Fe+Ti-composition as calculated in pMELTS in Table S5.

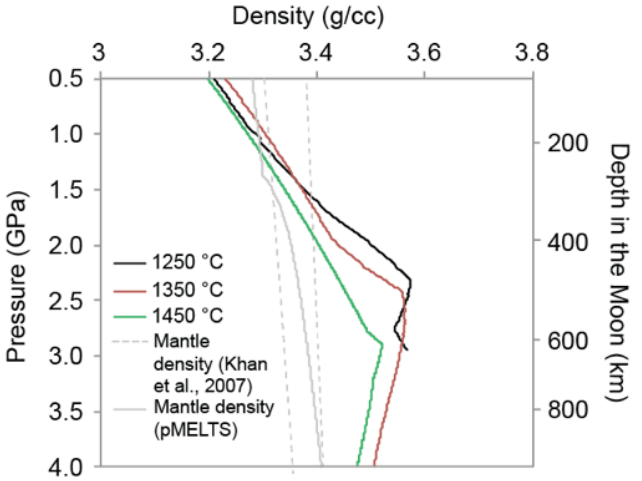

Figure S9. Density of isothermal Ti-rich melts as a function of pressure (left), or depth (right), at 1250 °C (black), 1350 °C (red), and 1450 °C (green), calculated by pMELTS. Melt composition starts at 0.5 GPa. Solid phases formed along the liquidus due to increasing pressure are fractionated before the next pressure step. The range of lunar mantle densities estimated by Khan et al. (2007) (gray dashed lines) bracket the mantle density estimated by pMELTS (solid gray line).

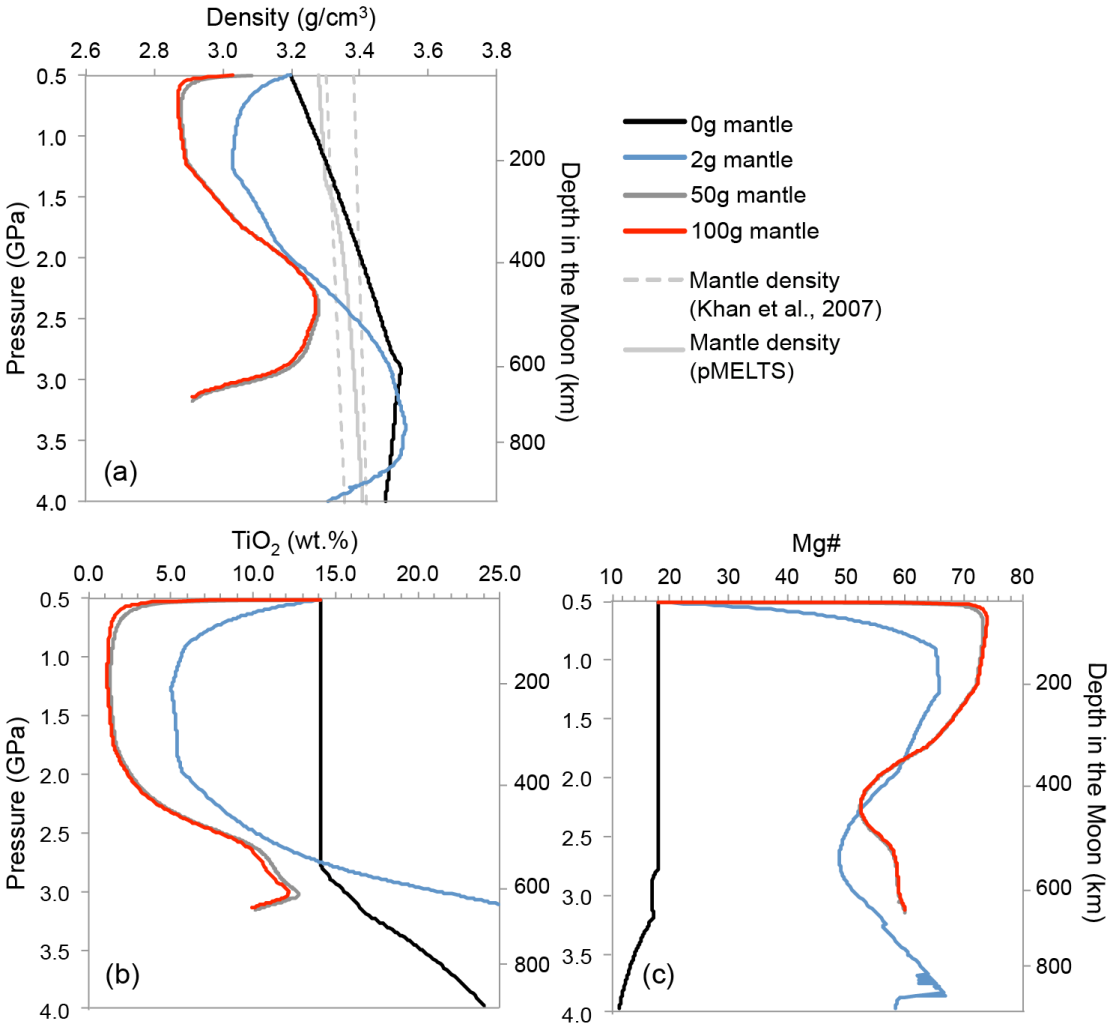

Figure S10. (a) Density of Fe+Ti-rich melts at 1450 °C, buffered at IW, for 0 g (black), 2 g (blue), 50 g (dark grey), and 100 g (red) of mantle assimilated with 100 g of Fe-Ti rich partial melt at each pressure-step of 0.005 GPa from 0.5 to 4 GPa. The composition of the Fe+Ti-rich melt at the starting pressure of 0.5 GPa is the same as reported in Table 1. See Figure S8-S9 for additional melt descriptions of this process. (b) TiO_2 concentration in weight percent, and (c) Mg# [molar MgO/(molar MgO+ molar FeO)×100] of Fe+Ti-rich melts at 1450 °C, buffered at IW, for 0 wt% (black), 2 wt% (blue), 50 wt% (dark grey), and 100 wt% (red) of mantle assimilated at each pressure-step of 0.005 GPa from 0.5 to 4 GPa. The composition of the Fe+Ti-rich melt at the starting pressure of 0.5 GPa is the same as reported in Table S5.

Table S6. Starting compositions used in modeling sinking of a Ti-rich partial melt through the lunar mantle.

Oxide	Ti-rich partial melt (wt. %)[a]	Lunar mantle (wt. %)[b]
SiO_2	36.70	44.40
TiO_2	14.20	0.31
Al_2O_3	4.00	6.14
Cr_2O_3	-	0.61
FeO	32.20	10.90
MnO	-	0.15
MgO	3.98	32.70
CaO	9.15	4.60
Na_2O	-	0.09
K_2O	-	0.01

[a] Partial melt of modeled Ti-rich cumulate from van Orman and Grove (2000). The melt was generated at 1.8 GPa, 1290 °C.
[b] Taylor (1982)

Text S1.2.1. Discussion: Impacts as a Melt Transport Mechanism

One potential mechanism to overcome this density barrier is for the Fe+Ti-rich material to be mechanically forced to higher pressures during cratering events. Material below the impact point is pushed deeper into the mantle during the formation of the transient crater, although often only momentarily before rebounding. The impact shock wave could also provide energy to re-melt an ilmenite layer. In order to allow percolation of ilmenite-rich melt to the CMB, material must have remained at pressures greater than the crossover pressure after the impact, either by permanent depression of material layers or by mixing with material deeper in the mantle, e.g., by Kelvin-Helmholtz instabilities. However, it is unlikely that impacts alone can transport enough ilmenite-rich material to depth to produce the proposed 150 km thick partially molten layer at the

CMB. It would require all impacts that produced craters >200 km (Head et al., 2010) to transport 50% of the ilmenite-rich-layer below the crater to pressures in excess of the density crossover for long enough for those melts to percolate deeper into the mantle. This is a highly unlikely scenario and so we discount impacts as a potential transport mechanism.

Text S1.2.2. Sinking of an Ilmenite-Rich Layer to the CMB as a Solid

Text S1.2.2.1 Methods: Convection Modeling

Another possible mechanism for transport of ilmenite-rich material to the CMB is by solid-state mantle convection. Here we study the physical process and rheology of mantle overturn, as well as the stability of a solid dense Fe+Ti-rich layer after overturn, using the ASPECT mantle convection code version 1.1 (http://aspect.dealii.org) (Kronbichler et al., 2012), see Table S4. We simulated a 2D annulus with a core radius of 330 km and a homogeneous mantle with the exception of an initially sub-crustal ilmenite layer. The initial density and thermal profile were set to the post-differentiation and solidification of the early magma ocean, i.e. ~0.2 Ga after formation of the Moon occurring at t = 0 Ga within our simulation. The simulation tested the persistence of the ilmenite-rich layer to the present day, ~4 Ga. ASPECT was originally created for the Earth where gravity is considered constant within the mantle. This is not the case for the Moon with a much smaller core. Therefore, we developed two new plugins for ASPECT to capture the physics of the mantle dynamics for this project: (1) a gravity function to calculate the changing lunar gravity over the mantle depths; and (2) boundary temperatures that vary with position and time. The latter was employed in the lower boundary temperature setting, such that the temperature of the core decreases with time. A list of all ASPECT model parameters is provided in Table S4.

The initial state was set to the post-differentiation and solidification of the early magma ocean, i.e. ~0.2 Ga after formation of the Moon occurring at 0 Ga in our model. The model started with a crustal ilmenite-rich dense layer (3,790 kg/m^3) at the top of the mantle at 1,640 km radius or 30 km thickness considering geometric effects. These capture the rheology of the crustal ilmenite-rich layer. We used a temperature-dependent viscosity of the form, $\eta(T) = \eta_0 \exp(\beta(T - T_0)/T_0)$, where β is the thermal viscosity exponent (we used β=9), and η_0 is the

reference viscosity at the reference temperature T_0. For the bulk mantle, we used a reference viscosity of 10^{21} Pa·s, density of 3400 kg/m^3, and temperature of 1600 K (*Laneuville et al.*, 2014). The lunar surface gravitational acceleration is g = 1.62 m/s^2. Gravity linearly decreased with depth: g = 1.58 m/s^2 at the top of the mantle, and g = 0.86 m/s^2 at the CMB. The boundary conditions for a hot early Moon are 1,673.15 K and 1,708.15 K at the top of the mantle and CMB, respectively. The ilmenite-rich layer contained a viscosity pre-factor of 10^{-3} Pa·s. This is lower than purposed in previous estimates (Elkins Tanton et al., 2002) and consistent with recent laboratory studies of dislocation creep flow laws (Dygert et al., 2016).

The CMB temperature decreased with time and was assumed to cool linearly. The time dependence was set such that the core reaches the estimated modern CMB temperature (1673.15 K) (Gagnepain-Beyneix et al., 2006) at current day. This is consistent within the selenotherms used in this project, see Figure 2. The initial CMB temperature decreased linearly with time as the core cooled. Following *Hagerty et al.*, (2006) for the estimated abundance of heat-producing elements within the lunar mantle, including a concentration of 0.039 ppm U, 0.15 ppm Th, and 212 ppm K, we estimated a radiogenic heating rate of 8.5e-12 W/kg. Adiabatic heating and heating from shear friction were considered negligible. The boundary conditions were free slip both at the surface and the CMB. We used a globally refined mesh without adaptive refinement.

Text S1.2.2.2 Results: Convection Modeling

The ASPECT lunar convection model shows that a dense, near-surface ilmenite-rich layer is gravitationally unstable and sinks toward the CMB on a timescale of ~100 Myr (Figure S11). We do not see any remnant of the original layer remaining at the top of the mantle after 4 Ga. The model shows some mixing of the dense ilmenite rich layer with mantle material; however, the majority sinks to form a ~150 km thick layer at the CMB with density of 3,435 kg/m^3 (Figure S11f, red colored layer) that persists throughout the 1 Ga of the model calculation. This confirms that the ilmenite-rich layer need not be partially molten during sinking to the CMB, contrary to Elkins-Tanton et al. (2002), and the viscosity of the solid ilmenite-rich layer is low enough for down dwellings to form. Longer runs (>1 Myr) also confirm the long term stability of the ilmenite layer at the CMB.

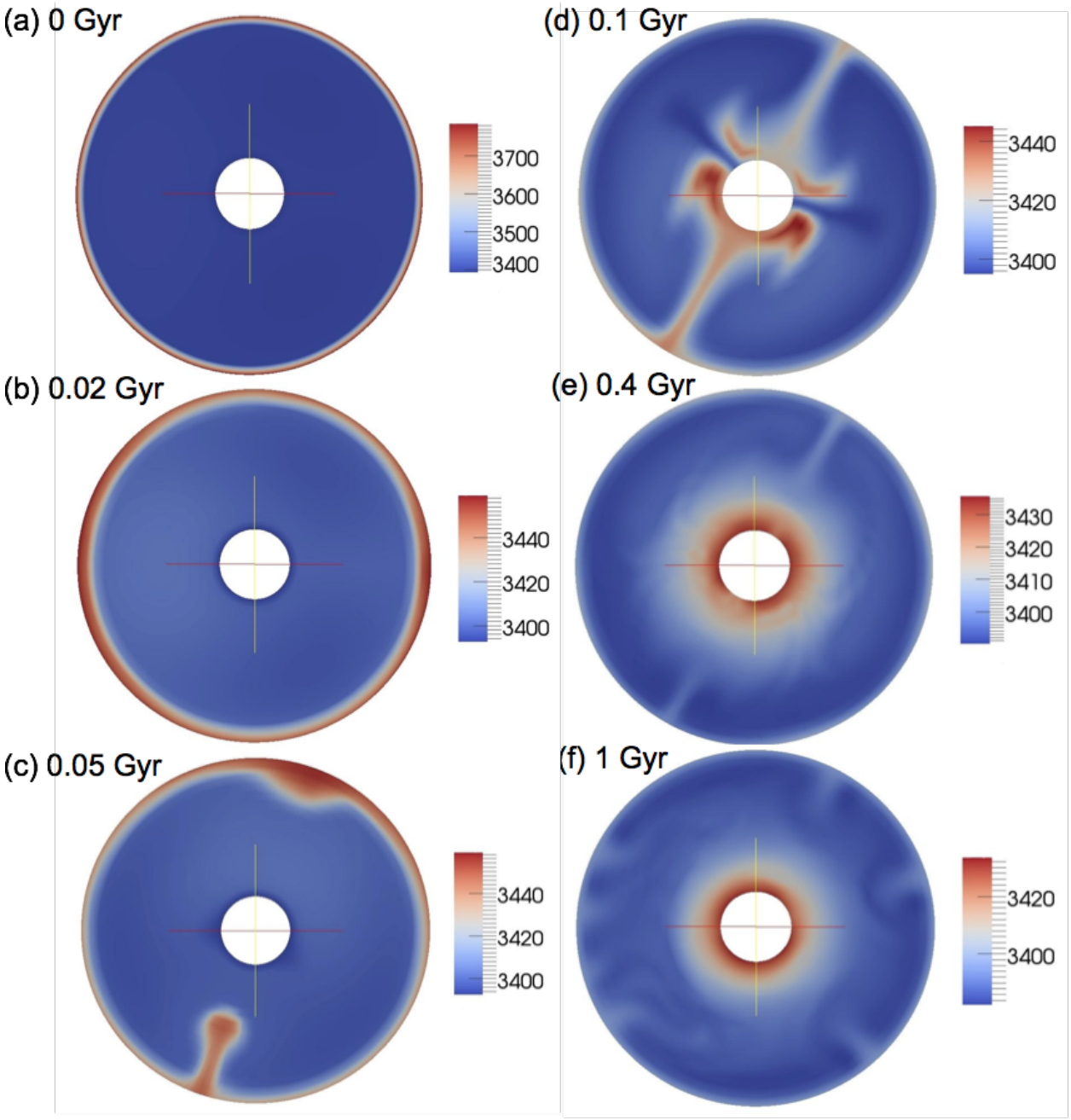

Figure S11. Snapshots of the 2D lunar mantle convection model presenting sections of density (given in kg/m^3). Initially, an ilmenite-rich layer with a thickness of 30 km is set on top of the mantle at radius of 1,640 km. Note the different color scales used at each time.

Text S1.3 Discussion

We find that both scenarios of no assimilation and impacts associated with high burial efficiency are unlikely to lead to the sinking of a partially molten, upper ilmenite-rich layer.

However, we observe that the upper ilmenite can sink as a solid during lunar mantle overturn (Section *S1.2.2.2*). Given that the viscosity of the ilmenite-rich layer is lower than olivine-rich mantle (Dygert et al., 2016), it is unnecessary to assume that viscosity is a constraint to downwelling in its solid state (Figure S11). After sinking, the ilmenite-rich layer at the CMB is found to be stable, at least up to 1 Ga since the onset of overturn. Therefore, our study affirms that the upper ilmenite can sink into the lower mantle, in accordance with the mantle overturn discussed in previous studies (Hess & Parmentier, 1995; Li et al., 2019; de Vries et al., 2010; Yu et al., 2019; Zhong et al., 2000).

Text S2. Model Count List by Subclass and Sigma

Text S2.1 Geophysics RMSND – CH-Hauri

39197 PassedModels_ModelA_Hauri_maxT_100000_sig-EQV-RMSND_geophy.dat
35077 PassedModels_ModelA_Hauri_maxT_1000_sig-EQV-RMSND_geophy.dat
4837 PassedModels_ModelA_Hauri_maxT_100_sig-EQV-RMSND_geophy.dat
620 PassedModels_ModelA_Hauri_maxT_10_sig-EQV-RMSND_geophy.dat
890 PassedModels_ModelA_Hauri_maxT_12_sig-EQV-RMSND_geophy.dat
1368 PassedModels_ModelA_Hauri_maxT_15_sig-EQV-RMSND_geophy.dat
11 PassedModels_ModelA_Hauri_maxT_1_sig-EQV-RMSND_geophy.dat
1982 PassedModels_ModelA_Hauri_maxT_20_sig-EQV-RMSND_geophy.dat
2352 PassedModels_ModelA_Hauri_maxT_25_sig-EQV-RMSND_geophy.dat
24 PassedModels_ModelA_Hauri_maxT_2_sig-EQV-RMSND_geophy.dat
63 PassedModels_ModelA_Hauri_maxT_3_sig-EQV-RMSND_geophy.dat
21259 PassedModels_ModelA_Hauri_maxT_500_sig-EQV-RMSND_geophy.dat
3564 PassedModels_ModelA_Hauri_maxT_50_sig-EQV-RMSND_geophy.dat
154 PassedModels_ModelA_Hauri_maxT_5_sig-EQV-RMSND_geophy.dat
405 PassedModels_ModelA_Hauri_maxT_8_sig-EQV-RMSND_geophy.dat

40494 PassedModels_ModelA_Hauri_meanT_100000_sig-EQV-RMSND_geophy.dat
36217 PassedModels_ModelA_Hauri_meanT_1000_sig-EQV-RMSND_geophy.dat
4891 PassedModels_ModelA_Hauri_meanT_100_sig-EQV-RMSND_geophy.dat
619 PassedModels_ModelA_Hauri_meanT_10_sig-EQV-RMSND_geophy.dat
874 PassedModels_ModelA_Hauri_meanT_12_sig-EQV-RMSND_geophy.dat
1247 PassedModels_ModelA_Hauri_meanT_15_sig-EQV-RMSND_geophy.dat
7 PassedModels_ModelA_Hauri_meanT_1_sig-EQV-RMSND_geophy.dat
1749 PassedModels_ModelA_Hauri_meanT_20_sig-EQV-RMSND_geophy.dat
2129 PassedModels_ModelA_Hauri_meanT_25_sig-EQV-RMSND_geophy.dat
19 PassedModels_ModelA_Hauri_meanT_2_sig-EQV-RMSND_geophy.dat
50 PassedModels_ModelA_Hauri_meanT_3_sig-EQV-RMSND_geophy.dat
19771 PassedModels_ModelA_Hauri_meanT_500_sig-EQV-RMSND_geophy.dat
3280 PassedModels_ModelA_Hauri_meanT_50_sig-EQV-RMSND_geophy.dat
140 PassedModels_ModelA_Hauri_meanT_5_sig-EQV-RMSND_geophy.dat
409 PassedModels_ModelA_Hauri_meanT_8_sig-EQV-RMSND_geophy.dat

46679 PassedModels_ModelA_Hauri_minT_100000_sig-EQV-RMSND_geophy.dat
41685 PassedModels_ModelA_Hauri_minT_1000_sig-EQV-RMSND_geophy.dat
5491 PassedModels_ModelA_Hauri_minT_100_sig-EQV-RMSND_geophy.dat
0 PassedModels_ModelA_Hauri_minT_10_sig-EQV-RMSND_geophy.dat
0 PassedModels_ModelA_Hauri_minT_12_sig-EQV-RMSND_geophy.dat
0 PassedModels_ModelA_Hauri_minT_15_sig-EQV-RMSND_geophy.dat
0 PassedModels_ModelA_Hauri_minT_1_sig-EQV-RMSND_geophy.dat

0 PassedModels_ModelA_Hauri_minT_20_sig-EQV-RMSND_geophy.dat
0 PassedModels_ModelA_Hauri_minT_25_sig-EQV-RMSND_geophy.dat
0 PassedModels_ModelA_Hauri_minT_2_sig-EQV-RMSND_geophy.dat
0 PassedModels_ModelA_Hauri_minT_3_sig-EQV-RMSND_geophy.dat
23086 PassedModels_ModelA_Hauri_minT_500_sig-EQV-RMSND_geophy.dat
2126 PassedModels_ModelA_Hauri_minT_50_sig-EQV-RMSND_geophy.dat
0 PassedModels_ModelA_Hauri_minT_5_sig-EQV-RMSND_geophy.dat
0 PassedModels_ModelA_Hauri_minT_8_sig-EQV-RMSND_geophy.dat

Text S2.2 Geophysics RMSND – CH-Taylor

40811 PassedModels_ModelA_Taylor_maxT_100000_sig-EQV-RMSND_geophy.dat
36715 PassedModels_ModelA_Taylor_maxT_1000_sig-EQV-RMSND_geophy.dat
5527 PassedModels_ModelA_Taylor_maxT_100_sig-EQV-RMSND_geophy.dat
631 PassedModels_ModelA_Taylor_maxT_10_sig-EQV-RMSND_geophy.dat
955 PassedModels_ModelA_Taylor_maxT_12_sig-EQV-RMSND_geophy.dat
1555 PassedModels_ModelA_Taylor_maxT_15_sig-EQV-RMSND_geophy.dat
5 PassedModels_ModelA_Taylor_maxT_1_sig-EQV-RMSND_geophy.dat
2499 PassedModels_ModelA_Taylor_maxT_20_sig-EQV-RMSND_geophy.dat
3223 PassedModels_ModelA_Taylor_maxT_25_sig-EQV-RMSND_geophy.dat
14 PassedModels_ModelA_Taylor_maxT_2_sig-EQV-RMSND_geophy.dat
36 PassedModels_ModelA_Taylor_maxT_3_sig-EQV-RMSND_geophy.dat
21669 PassedModels_ModelA_Taylor_maxT_500_sig-EQV-RMSND_geophy.dat
4435 PassedModels_ModelA_Taylor_maxT_50_sig-EQV-RMSND_geophy.dat
137 PassedModels_ModelA_Taylor_maxT_5_sig-EQV-RMSND_geophy.dat
386 PassedModels_ModelA_Taylor_maxT_8_sig-EQV-RMSND_geophy.dat

44871 PassedModels_ModelA_Taylor_meanT_100000_sig-EQV-RMSND_geophy.dat
40298 PassedModels_ModelA_Taylor_meanT_1000_sig-EQV-RMSND_geophy.dat
4629 PassedModels_ModelA_Taylor_meanT_100_sig-EQV-RMSND_geophy.dat
0 PassedModels_ModelA_Taylor_meanT_10_sig-EQV-RMSND_geophy.dat
0 PassedModels_ModelA_Taylor_meanT_12_sig-EQV-RMSND_geophy.dat
0 PassedModels_ModelA_Taylor_meanT_15_sig-EQV-RMSND_geophy.dat
0 PassedModels_ModelA_Taylor_meanT_1_sig-EQV-RMSND_geophy.dat
0 PassedModels_ModelA_Taylor_meanT_20_sig-EQV-RMSND_geophy.dat
0 PassedModels_ModelA_Taylor_meanT_25_sig-EQV-RMSND_geophy.dat
0 PassedModels_ModelA_Taylor_meanT_2_sig-EQV-RMSND_geophy.dat
0 PassedModels_ModelA_Taylor_meanT_3_sig-EQV-RMSND_geophy.dat
22716 PassedModels_ModelA_Taylor_meanT_500_sig-EQV-RMSND_geophy.dat

88 PassedModels_ModelA_Taylor_meanT_50_sig-EQV-RMSND_geophy.dat
0 PassedModels_ModelA_Taylor_meanT_5_sig-EQV-RMSND_geophy.dat
0 PassedModels_ModelA_Taylor_meanT_8_sig-EQV-RMSND_geophy.dat

49801 PassedModels_ModelA_Taylor_minT_100000_sig-EQV-RMSND_geophy.dat
44672 PassedModels_ModelA_Taylor_minT_1000_sig-EQV-RMSND_geophy.dat
0 PassedModels_ModelA_Taylor_minT_100_sig-EQV-RMSND_geophy.dat
0 PassedModels_ModelA_Taylor_minT_10_sig-EQV-RMSND_geophy.dat
0 PassedModels_ModelA_Taylor_minT_12_sig-EQV-RMSND_geophy.dat
0 PassedModels_ModelA_Taylor_minT_15_sig-EQV-RMSND_geophy.dat
0 PassedModels_ModelA_Taylor_minT_1_sig-EQV-RMSND_geophy.dat
0 PassedModels_ModelA_Taylor_minT_20_sig-EQV-RMSND_geophy.dat
0 PassedModels_ModelA_Taylor_minT_25_sig-EQV-RMSND_geophy.dat
0 PassedModels_ModelA_Taylor_minT_2_sig-EQV-RMSND_geophy.dat
0 PassedModels_ModelA_Taylor_minT_3_sig-EQV-RMSND_geophy.dat
25235 PassedModels_ModelA_Taylor_minT_500_sig-EQV-RMSND_geophy.dat
0 PassedModels_ModelA_Taylor_minT_50_sig-EQV-RMSND_geophy.dat
0 PassedModels_ModelA_Taylor_minT_5_sig-EQV-RMSND_geophy.dat
0 PassedModels_ModelA_Taylor_minT_8_sig-EQV-RMSND_geophy.dat

Text S2.3 Geophysics RMSND – CS

37533 PassedModels_ModelB_Orig_maxT_100000_sig-EQV-RMSND_geophy.dat
34287 PassedModels_ModelB_Orig_maxT_1000_sig-EQV-RMSND_geophy.dat
6374 PassedModels_ModelB_Orig_maxT_100_sig-EQV-RMSND_geophy.dat
439 PassedModels_ModelB_Orig_maxT_10_sig-EQV-RMSND_geophy.dat
662 PassedModels_ModelB_Orig_maxT_12_sig-EQV-RMSND_geophy.dat
990 PassedModels_ModelB_Orig_maxT_15_sig-EQV-RMSND_geophy.dat
6 PassedModels_ModelB_Orig_maxT_1_sig-EQV-RMSND_geophy.dat
1653 PassedModels_ModelB_Orig_maxT_20_sig-EQV-RMSND_geophy.dat
2339 PassedModels_ModelB_Orig_maxT_25_sig-EQV-RMSND_geophy.dat
19 PassedModels_ModelB_Orig_maxT_2_sig-EQV-RMSND_geophy.dat
34 PassedModels_ModelB_Orig_maxT_3_sig-EQV-RMSND_geophy.dat
19151 PassedModels_ModelB_Orig_maxT_500_sig-EQV-RMSND_geophy.dat
4416 PassedModels_ModelB_Orig_maxT_50_sig-EQV-RMSND_geophy.dat
85 PassedModels_ModelB_Orig_maxT_5_sig-EQV-RMSND_geophy.dat
271 PassedModels_ModelB_Orig_maxT_8_sig-EQV-RMSND_geophy.dat

42667 PassedModels_ModelB_Orig_meanT_100000_sig-EQV-RMSND_geophy.dat
39172 PassedModels_ModelB_Orig_meanT_1000_sig-EQV-RMSND_geophy.dat
7051 PassedModels_ModelB_Orig_meanT_100_sig-EQV-RMSND_geophy.dat
354 PassedModels_ModelB_Orig_meanT_10_sig-EQV-RMSND_geophy.dat
494 PassedModels_ModelB_Orig_meanT_12_sig-EQV-RMSND_geophy.dat
701 PassedModels_ModelB_Orig_meanT_15_sig-EQV-RMSND_geophy.dat
5 PassedModels_ModelB_Orig_meanT_1_sig-EQV-RMSND_geophy.dat
1087 PassedModels_ModelB_Orig_meanT_20_sig-EQV-RMSND_geophy.dat
1439 PassedModels_ModelB_Orig_meanT_25_sig-EQV-RMSND_geophy.dat
16 PassedModels_ModelB_Orig_meanT_2_sig-EQV-RMSND_geophy.dat
40 PassedModels_ModelB_Orig_meanT_3_sig-EQV-RMSND_geophy.dat
22375 PassedModels_ModelB_Orig_meanT_500_sig-EQV-RMSND_geophy.dat
2777 PassedModels_ModelB_Orig_meanT_50_sig-EQV-RMSND_geophy.dat
82 PassedModels_ModelB_Orig_meanT_5_sig-EQV-RMSND_geophy.dat
216 PassedModels_ModelB_Orig_meanT_8_sig-EQV-RMSND_geophy.dat

41189 PassedModels_ModelB_Orig_minT_100000_sig-EQV-RMSND_geophy.dat
37527 PassedModels_ModelB_Orig_minT_1000_sig-EQV-RMSND_geophy.dat
6095 PassedModels_ModelB_Orig_minT_100_sig-EQV-RMSND_geophy.dat
361 PassedModels_ModelB_Orig_minT_10_sig-EQV-RMSND_geophy.dat
513 PassedModels_ModelB_Orig_minT_12_sig-EQV-RMSND_geophy.dat
749 PassedModels_ModelB_Orig_minT_15_sig-EQV-RMSND_geophy.dat
8 PassedModels_ModelB_Orig_minT_1_sig-EQV-RMSND_geophy.dat
1191 PassedModels_ModelB_Orig_minT_20_sig-EQV-RMSND_geophy.dat
1622 PassedModels_ModelB_Orig_minT_25_sig-EQV-RMSND_geophy.dat
22 PassedModels_ModelB_Orig_minT_2_sig-EQV-RMSND_geophy.dat
61 PassedModels_ModelB_Orig_minT_3_sig-EQV-RMSND_geophy.dat
19354 PassedModels_ModelB_Orig_minT_500_sig-EQV-RMSND_geophy.dat
2888 PassedModels_ModelB_Orig_minT_50_sig-EQV-RMSND_geophy.dat
128 PassedModels_ModelB_Orig_minT_5_sig-EQV-RMSND_geophy.dat
222 PassedModels_ModelB_Orig_minT_8_sig-EQV-RMSND_geophy.dat

Text S2.4 BC-RMSND – CH-Hauri

39197 PassedModels_ModelA_Hauri_maxT_100000_sig-EQV-RMSND_bulkchem.dat
35073 PassedModels_ModelA_Hauri_maxT_1000_sig-EQV-RMSND_bulkchem.dat
4780 PassedModels_ModelA_Hauri_maxT_100_sig-EQV-RMSND_bulkchem.dat
165 PassedModels_ModelA_Hauri_maxT_10_sig-EQV-RMSND_bulkchem.dat
317 PassedModels_ModelA_Hauri_maxT_12_sig-EQV-RMSND_bulkchem.dat
741 PassedModels_ModelA_Hauri_maxT_15_sig-EQV-RMSND_bulkchem.dat
0 PassedModels_ModelA_Hauri_maxT_1_sig-EQV-RMSND_bulkchem.dat
1651 PassedModels_ModelA_Hauri_maxT_20_sig-EQV-RMSND_bulkchem.dat
2197 PassedModels_ModelA_Hauri_maxT_25_sig-EQV-RMSND_bulkchem.dat
0 PassedModels_ModelA_Hauri_maxT_2_sig-EQV-RMSND_bulkchem.dat
0 PassedModels_ModelA_Hauri_maxT_3_sig-EQV-RMSND_bulkchem.dat
21120 PassedModels_ModelA_Hauri_maxT_500_sig-EQV-RMSND_bulkchem.dat
3547 PassedModels_ModelA_Hauri_maxT_50_sig-EQV-RMSND_bulkchem.dat
0 PassedModels_ModelA_Hauri_maxT_5_sig-EQV-RMSND_bulkchem.dat
63 PassedModels_ModelA_Hauri_maxT_8_sig-EQV-RMSND_bulkchem.dat

40494 PassedModels_ModelA_Hauri_meanT_100000_sig-EQV-RMSND_bulkchem.dat
36216 PassedModels_ModelA_Hauri_meanT_1000_sig-EQV-RMSND_bulkchem.dat
4881 PassedModels_ModelA_Hauri_meanT_100_sig-EQV-RMSND_bulkchem.dat
451 PassedModels_ModelA_Hauri_meanT_10_sig-EQV-RMSND_bulkchem.dat
726 PassedModels_ModelA_Hauri_meanT_12_sig-EQV-RMSND_bulkchem.dat
1133 PassedModels_ModelA_Hauri_meanT_15_sig-EQV-RMSND_bulkchem.dat
0 PassedModels_ModelA_Hauri_meanT_1_sig-EQV-RMSND_bulkchem.dat
1700 PassedModels_ModelA_Hauri_meanT_20_sig-EQV-RMSND_bulkchem.dat
2103 PassedModels_ModelA_Hauri_meanT_25_sig-EQV-RMSND_bulkchem.dat
0 PassedModels_ModelA_Hauri_meanT_2_sig-EQV-RMSND_bulkchem.dat
9 PassedModels_ModelA_Hauri_meanT_3_sig-EQV-RMSND_bulkchem.dat
19677 PassedModels_ModelA_Hauri_meanT_500_sig-EQV-RMSND_bulkchem.dat
3270 PassedModels_ModelA_Hauri_meanT_50_sig-EQV-RMSND_bulkchem.dat
47 PassedModels_ModelA_Hauri_meanT_5_sig-EQV-RMSND_bulkchem.dat
244 PassedModels_ModelA_Hauri_meanT_8_sig-EQV-RMSND_bulkchem.dat

46679 PassedModels_ModelA_Hauri_minT_100000_sig-EQV-RMSND_bulkchem.dat
41656 PassedModels_ModelA_Hauri_minT_1000_sig-EQV-RMSND_bulkchem.dat
5489 PassedModels_ModelA_Hauri_minT_100_sig-EQV-RMSND_bulkchem.dat
0 PassedModels_ModelA_Hauri_minT_10_sig-EQV-RMSND_bulkchem.dat
0 PassedModels_ModelA_Hauri_minT_12_sig-EQV-RMSND_bulkchem.dat
0 PassedModels_ModelA_Hauri_minT_15_sig-EQV-RMSND_bulkchem.dat
0 PassedModels_ModelA_Hauri_minT_1_sig-EQV-RMSND_bulkchem.dat
0 PassedModels_ModelA_Hauri_minT_20_sig-EQV-RMSND_bulkchem.dat
0 PassedModels_ModelA_Hauri_minT_25_sig-EQV-RMSND_bulkchem.dat
0 PassedModels_ModelA_Hauri_minT_2_sig-EQV-RMSND_bulkchem.dat
0 PassedModels_ModelA_Hauri_minT_3_sig-EQV-RMSND_bulkchem.dat
23034 PassedModels_ModelA_Hauri_minT_500_sig-EQV-RMSND_bulkchem.dat

2119 PassedModels_ModelA_Hauri_minT_50_sig-EQV-RMSND_bulkchem.dat
0 PassedModels_ModelA_Hauri_minT_5_sig-EQV-RMSND_bulkchem.dat
0 PassedModels_ModelA_Hauri_minT_8_sig-EQV-RMSND_bulkchem.dat

Text S2.5 BC-RMSND – CH-Taylor

40811 PassedModels_ModelA_Taylor_maxT_100000_sig-EQV-RMSND_bulkchem.dat
36714 PassedModels_ModelA_Taylor_maxT_1000_sig-EQV-RMSND_bulkchem.dat
5518 PassedModels_ModelA_Taylor_maxT_100_sig-EQV-RMSND_bulkchem.dat
566 PassedModels_ModelA_Taylor_maxT_10_sig-EQV-RMSND_bulkchem.dat
867 PassedModels_ModelA_Taylor_maxT_12_sig-EQV-RMSND_bulkchem.dat
1485 PassedModels_ModelA_Taylor_maxT_15_sig-EQV-RMSND_bulkchem.dat
0 PassedModels_ModelA_Taylor_maxT_1_sig-EQV-RMSND_bulkchem.dat
2449 PassedModels_ModelA_Taylor_maxT_20_sig-EQV-RMSND_bulkchem.dat
3195 PassedModels_ModelA_Taylor_maxT_25_sig-EQV-RMSND_bulkchem.dat
7 PassedModels_ModelA_Taylor_maxT_2_sig-EQV-RMSND_bulkchem.dat
20 PassedModels_ModelA_Taylor_maxT_3_sig-EQV-RMSND_bulkchem.dat
21534 PassedModels_ModelA_Taylor_maxT_500_sig-EQV-RMSND_bulkchem.dat
4430 PassedModels_ModelA_Taylor_maxT_50_sig-EQV-RMSND_bulkchem.dat
98 PassedModels_ModelA_Taylor_maxT_5_sig-EQV-RMSND_bulkchem.dat
307 PassedModels_ModelA_Taylor_maxT_8_sig-EQV-RMSND_bulkchem.dat

44871 PassedModels_ModelA_Taylor_meanT_100000_sig-EQV-RMSND_bulkchem.dat
40280 PassedModels_ModelA_Taylor_meanT_1000_sig-EQV-RMSND_bulkchem.dat
4628 PassedModels_ModelA_Taylor_meanT_100_sig-EQV-RMSND_bulkchem.dat
0 PassedModels_ModelA_Taylor_meanT_10_sig-EQV-RMSND_bulkchem.dat
0 PassedModels_ModelA_Taylor_meanT_12_sig-EQV-RMSND_bulkchem.dat
0 PassedModels_ModelA_Taylor_meanT_15_sig-EQV-RMSND_bulkchem.dat
0 PassedModels_ModelA_Taylor_meanT_1_sig-EQV-RMSND_bulkchem.dat
0 PassedModels_ModelA_Taylor_meanT_20_sig-EQV-RMSND_bulkchem.dat
0 PassedModels_ModelA_Taylor_meanT_25_sig-EQV-RMSND_bulkchem.dat
0 PassedModels_ModelA_Taylor_meanT_2_sig-EQV-RMSND_bulkchem.dat
0 PassedModels_ModelA_Taylor_meanT_3_sig-EQV-RMSND_bulkchem.dat
22600 PassedModels_ModelA_Taylor_meanT_500_sig-EQV-RMSND_bulkchem.dat
83 PassedModels_ModelA_Taylor_meanT_50_sig-EQV-RMSND_bulkchem.dat
0 PassedModels_ModelA_Taylor_meanT_5_sig-EQV-RMSND_bulkchem.dat
0 PassedModels_ModelA_Taylor_meanT_8_sig-EQV-RMSND_bulkchem.dat

49801 PassedModels_ModelA_Taylor_minT_100000_sig-EQV-RMSND_bulkchem.dat

44654 PassedModels_ModelA_Taylor_minT_1000_sig-EQV-RMSND_bulkchem.dat
0 PassedModels_ModelA_Taylor_minT_100_sig-EQV-RMSND_bulkchem.dat
0 PassedModels_ModelA_Taylor_minT_10_sig-EQV-RMSND_bulkchem.dat
0 PassedModels_ModelA_Taylor_minT_12_sig-EQV-RMSND_bulkchem.dat
0 PassedModels_ModelA_Taylor_minT_15_sig-EQV-RMSND_bulkchem.dat
0 PassedModels_ModelA_Taylor_minT_1_sig-EQV-RMSND_bulkchem.dat
0 PassedModels_ModelA_Taylor_minT_20_sig-EQV-RMSND_bulkchem.dat
0 PassedModels_ModelA_Taylor_minT_25_sig-EQV-RMSND_bulkchem.dat
0 PassedModels_ModelA_Taylor_minT_2_sig-EQV-RMSND_bulkchem.dat
0 PassedModels_ModelA_Taylor_minT_3_sig-EQV-RMSND_bulkchem.dat
25175 PassedModels_ModelA_Taylor_minT_500_sig-EQV-RMSND_bulkchem.dat
0 PassedModels_ModelA_Taylor_minT_50_sig-EQV-RMSND_bulkchem.dat
0 PassedModels_ModelA_Taylor_minT_5_sig-EQV-RMSND_bulkchem.dat
0 PassedModels_ModelA_Taylor_minT_8_sig-EQV-RMSND_bulkchem.dat

Text S2.6 BC-RMSND – CS

37533 PassedModels_ModelB_Orig_maxT_100000_sig-EQV-RMSND_bulkchem.dat
34287 PassedModels_ModelB_Orig_maxT_1000_sig-EQV-RMSND_bulkchem.dat
6361 PassedModels_ModelB_Orig_maxT_100_sig-EQV-RMSND_bulkchem.dat
239 PassedModels_ModelB_Orig_maxT_10_sig-EQV-RMSND_bulkchem.dat
414 PassedModels_ModelB_Orig_maxT_12_sig-EQV-RMSND_bulkchem.dat
735 PassedModels_ModelB_Orig_maxT_15_sig-EQV-RMSND_bulkchem.dat
0 PassedModels_ModelB_Orig_maxT_1_sig-EQV-RMSND_bulkchem.dat
1460 PassedModels_ModelB_Orig_maxT_20_sig-EQV-RMSND_bulkchem.dat
2185 PassedModels_ModelB_Orig_maxT_25_sig-EQV-RMSND_bulkchem.dat
0 PassedModels_ModelB_Orig_maxT_2_sig-EQV-RMSND_bulkchem.dat
0 PassedModels_ModelB_Orig_maxT_3_sig-EQV-RMSND_bulkchem.dat
19075 PassedModels_ModelB_Orig_maxT_500_sig-EQV-RMSND_bulkchem.dat
4379 PassedModels_ModelB_Orig_maxT_50_sig-EQV-RMSND_bulkchem.dat
16 PassedModels_ModelB_Orig_maxT_5_sig-EQV-RMSND_bulkchem.dat
115 PassedModels_ModelB_Orig_maxT_8_sig-EQV-RMSND_bulkchem.dat

42667 PassedModels_ModelB_Orig_meanT_100000_sig-EQV-RMSND_bulkchem.dat
39154 PassedModels_ModelB_Orig_meanT_1000_sig-EQV-RMSND_bulkchem.dat
7026 PassedModels_ModelB_Orig_meanT_100_sig-EQV-RMSND_bulkchem.dat
202 PassedModels_ModelB_Orig_meanT_10_sig-EQV-RMSND_bulkchem.dat
353 PassedModels_ModelB_Orig_meanT_12_sig-EQV-RMSND_bulkchem.dat
595 PassedModels_ModelB_Orig_meanT_15_sig-EQV-RMSND_bulkchem.dat

0 PassedModels_ModelB_Orig_meanT_1_sig-EQV-RMSND_bulkchem.dat
1010 PassedModels_ModelB_Orig_meanT_20_sig-EQV-RMSND_bulkchem.dat
1395 PassedModels_ModelB_Orig_meanT_25_sig-EQV-RMSND_bulkchem.dat
0 PassedModels_ModelB_Orig_meanT_2_sig-EQV-RMSND_bulkchem.dat
0 PassedModels_ModelB_Orig_meanT_3_sig-EQV-RMSND_bulkchem.dat
22336 PassedModels_ModelB_Orig_meanT_500_sig-EQV-RMSND_bulkchem.dat
2767 PassedModels_ModelB_Orig_meanT_50_sig-EQV-RMSND_bulkchem.dat
14 PassedModels_ModelB_Orig_meanT_5_sig-EQV-RMSND_bulkchem.dat
83 PassedModels_ModelB_Orig_meanT_8_sig-EQV-RMSND_bulkchem.dat

41189 PassedModels_ModelB_Orig_minT_100000_sig-EQV-RMSND_bulkchem.dat
37515 PassedModels_ModelB_Orig_minT_1000_sig-EQV-RMSND_bulkchem.dat
6071 PassedModels_ModelB_Orig_minT_100_sig-EQV-RMSND_bulkchem.dat
247 PassedModels_ModelB_Orig_minT_10_sig-EQV-RMSND_bulkchem.dat
442 PassedModels_ModelB_Orig_minT_12_sig-EQV-RMSND_bulkchem.dat
680 PassedModels_ModelB_Orig_minT_15_sig-EQV-RMSND_bulkchem.dat
0 PassedModels_ModelB_Orig_minT_1_sig-EQV-RMSND_bulkchem.dat
1139 PassedModels_ModelB_Orig_minT_20_sig-EQV-RMSND_bulkchem.dat
1586 PassedModels_ModelB_Orig_minT_25_sig-EQV-RMSND_bulkchem.dat
0 PassedModels_ModelB_Orig_minT_2_sig-EQV-RMSND_bulkchem.dat
0 PassedModels_ModelB_Orig_minT_3_sig-EQV-RMSND_bulkchem.dat
19325 PassedModels_ModelB_Orig_minT_500_sig-EQV-RMSND_bulkchem.dat
2883 PassedModels_ModelB_Orig_minT_50_sig-EQV-RMSND_bulkchem.dat
13 PassedModels_ModelB_Orig_minT_5_sig-EQV-RMSND_bulkchem.dat
164 PassedModels_ModelB_Orig_minT_8_sig-EQV-RMSND_bulkchem.dat

Text S2.7 Comb-RMSND – CH-Hauri

39197 PassedModels_ModelA_Hauri_maxT_100000_sig-EQV-RMSND_geophy-bulkchem.dat
35073 PassedModels_ModelA_Hauri_maxT_1000_sig-EQV-RMSND_geophy-bulkchem.dat
4780 PassedModels_ModelA_Hauri_maxT_100_sig-EQV-RMSND_geophy-bulkchem.dat
165 PassedModels_ModelA_Hauri_maxT_10_sig-EQV-RMSND_geophy-bulkchem.dat
317 PassedModels_ModelA_Hauri_maxT_12_sig-EQV-RMSND_geophy-bulkchem.dat
741 PassedModels_ModelA_Hauri_maxT_15_sig-EQV-RMSND_geophy-bulkchem.dat
0 PassedModels_ModelA_Hauri_maxT_1_sig-EQV-RMSND_geophy-bulkchem.dat
1651 PassedModels_ModelA_Hauri_maxT_20_sig-EQV-RMSND_geophy-bulkchem.dat
2197 PassedModels_ModelA_Hauri_maxT_25_sig-EQV-RMSND_geophy-bulkchem.dat
0 PassedModels_ModelA_Hauri_maxT_2_sig-EQV-RMSND_geophy-bulkchem.dat
0 PassedModels_ModelA_Hauri_maxT_3_sig-EQV-RMSND_geophy-bulkchem.dat
21120 PassedModels_ModelA_Hauri_maxT_500_sig-EQV-RMSND_geophy-bulkchem.dat

3547 PassedModels_ModelA_Hauri_maxT_50_sig-EQV-RMSND_geophy-bulkchem.dat
0 PassedModels_ModelA_Hauri_maxT_5_sig-EQV-RMSND_geophy-bulkchem.dat
63 PassedModels_ModelA_Hauri_maxT_8_sig-EQV-RMSND_geophy-bulkchem.dat

40494 PassedModels_ModelA_Hauri_meanT_100000_sig-EQV-RMSND_geophy-bulkchem.dat
36216 PassedModels_ModelA_Hauri_meanT_1000_sig-EQV-RMSND_geophy-bulkchem.dat
4881 PassedModels_ModelA_Hauri_meanT_100_sig-EQV-RMSND_geophy-bulkchem.dat
451 PassedModels_ModelA_Hauri_meanT_10_sig-EQV-RMSND_geophy-bulkchem.dat
726 PassedModels_ModelA_Hauri_meanT_12_sig-EQV-RMSND_geophy-bulkchem.dat
1133 PassedModels_ModelA_Hauri_meanT_15_sig-EQV-RMSND_geophy-bulkchem.dat
0 PassedModels_ModelA_Hauri_meanT_1_sig-EQV-RMSND_geophy-bulkchem.dat
1700 PassedModels_ModelA_Hauri_meanT_20_sig-EQV-RMSND_geophy-bulkchem.dat
2103 PassedModels_ModelA_Hauri_meanT_25_sig-EQV-RMSND_geophy-bulkchem.dat
0 PassedModels_ModelA_Hauri_meanT_2_sig-EQV-RMSND_geophy-bulkchem.dat
9 PassedModels_ModelA_Hauri_meanT_3_sig-EQV-RMSND_geophy-bulkchem.dat
19677 PassedModels_ModelA_Hauri_meanT_500_sig-EQV-RMSND_geophy-bulkchem.dat
3270 PassedModels_ModelA_Hauri_meanT_50_sig-EQV-RMSND_geophy-bulkchem.dat
47 PassedModels_ModelA_Hauri_meanT_5_sig-EQV-RMSND_geophy-bulkchem.dat
244 PassedModels_ModelA_Hauri_meanT_8_sig-EQV-RMSND_geophy-bulkchem.dat

46679 PassedModels_ModelA_Hauri_minT_100000_sig-EQV-RMSND_geophy-bulkchem.dat
41656 PassedModels_ModelA_Hauri_minT_1000_sig-EQV-RMSND_geophy-bulkchem.dat
5489 PassedModels_ModelA_Hauri_minT_100_sig-EQV-RMSND_geophy-bulkchem.dat
0 PassedModels_ModelA_Hauri_minT_10_sig-EQV-RMSND_geophy-bulkchem.dat
0 PassedModels_ModelA_Hauri_minT_12_sig-EQV-RMSND_geophy-bulkchem.dat
0 PassedModels_ModelA_Hauri_minT_15_sig-EQV-RMSND_geophy-bulkchem.dat
0 PassedModels_ModelA_Hauri_minT_1_sig-EQV-RMSND_geophy-bulkchem.dat
0 PassedModels_ModelA_Hauri_minT_20_sig-EQV-RMSND_geophy-bulkchem.dat
0 PassedModels_ModelA_Hauri_minT_25_sig-EQV-RMSND_geophy-bulkchem.dat
0 PassedModels_ModelA_Hauri_minT_2_sig-EQV-RMSND_geophy-bulkchem.dat
0 PassedModels_ModelA_Hauri_minT_3_sig-EQV-RMSND_geophy-bulkchem.dat
23034 PassedModels_ModelA_Hauri_minT_500_sig-EQV-RMSND_geophy-bulkchem.dat
2119 PassedModels_ModelA_Hauri_minT_50_sig-EQV-RMSND_geophy-bulkchem.dat
0 PassedModels_ModelA_Hauri_minT_5_sig-EQV-RMSND_geophy-bulkchem.dat
0 PassedModels_ModelA_Hauri_minT_8_sig-EQV-RMSND_geophy-bulkchem.dat

Text S2.8 Comb-RMSND – CH-Taylor

40811 PassedModels_ModelA_Taylor_maxT_100000_sig-EQV-RMSND_geophy-bulkchem.dat
36714 PassedModels_ModelA_Taylor_maxT_1000_sig-EQV-RMSND_geophy-bulkchem.dat
5518 PassedModels_ModelA_Taylor_maxT_100_sig-EQV-RMSND_geophy-bulkchem.dat
566 PassedModels_ModelA_Taylor_maxT_10_sig-EQV-RMSND_geophy-bulkchem.dat
867 PassedModels_ModelA_Taylor_maxT_12_sig-EQV-RMSND_geophy-bulkchem.dat
1485 PassedModels_ModelA_Taylor_maxT_15_sig-EQV-RMSND_geophy-bulkchem.dat
0 PassedModels_ModelA_Taylor_maxT_1_sig-EQV-RMSND_geophy-bulkchem.dat
2449 PassedModels_ModelA_Taylor_maxT_20_sig-EQV-RMSND_geophy-bulkchem.dat
3195 PassedModels_ModelA_Taylor_maxT_25_sig-EQV-RMSND_geophy-bulkchem.dat
7 PassedModels_ModelA_Taylor_maxT_2_sig-EQV-RMSND_geophy-bulkchem.dat
20 PassedModels_ModelA_Taylor_maxT_3_sig-EQV-RMSND_geophy-bulkchem.dat
21534 PassedModels_ModelA_Taylor_maxT_500_sig-EQV-RMSND_geophy-bulkchem.dat
4430 PassedModels_ModelA_Taylor_maxT_50_sig-EQV-RMSND_geophy-bulkchem.dat
98 PassedModels_ModelA_Taylor_maxT_5_sig-EQV-RMSND_geophy-bulkchem.dat
307 PassedModels_ModelA_Taylor_maxT_8_sig-EQV-RMSND_geophy-bulkchem.dat

44871 PassedModels_ModelA_Taylor_meanT_100000_sig-EQV-RMSND_geophy-bulkchem.dat
40280 PassedModels_ModelA_Taylor_meanT_1000_sig-EQV-RMSND_geophy-bulkchem.dat
4628 PassedModels_ModelA_Taylor_meanT_100_sig-EQV-RMSND_geophy-bulkchem.dat
0 PassedModels_ModelA_Taylor_meanT_10_sig-EQV-RMSND_geophy-bulkchem.dat
0 PassedModels_ModelA_Taylor_meanT_12_sig-EQV-RMSND_geophy-bulkchem.dat
0 PassedModels_ModelA_Taylor_meanT_15_sig-EQV-RMSND_geophy-bulkchem.dat
0 PassedModels_ModelA_Taylor_meanT_1_sig-EQV-RMSND_geophy-bulkchem.dat
0 PassedModels_ModelA_Taylor_meanT_20_sig-EQV-RMSND_geophy-bulkchem.dat
0 PassedModels_ModelA_Taylor_meanT_25_sig-EQV-RMSND_geophy-bulkchem.dat
0 PassedModels_ModelA_Taylor_meanT_2_sig-EQV-RMSND_geophy-bulkchem.dat
0 PassedModels_ModelA_Taylor_meanT_3_sig-EQV-RMSND_geophy-bulkchem.dat
22600 PassedModels_ModelA_Taylor_meanT_500_sig-EQV-RMSND_geophy-bulkchem.dat
83 PassedModels_ModelA_Taylor_meanT_50_sig-EQV-RMSND_geophy-bulkchem.dat
0 PassedModels_ModelA_Taylor_meanT_5_sig-EQV-RMSND_geophy-bulkchem.dat
0 PassedModels_ModelA_Taylor_meanT_8_sig-EQV-RMSND_geophy-bulkchem.dat

49801 PassedModels_ModelA_Taylor_minT_100000_sig-EQV-RMSND_geophy-bulkchem.dat
44654 PassedModels_ModelA_Taylor_minT_1000_sig-EQV-RMSND_geophy-bulkchem.dat
0 PassedModels_ModelA_Taylor_minT_100_sig-EQV-RMSND_geophy-bulkchem.dat
0 PassedModels_ModelA_Taylor_minT_10_sig-EQV-RMSND_geophy-bulkchem.dat
0 PassedModels_ModelA_Taylor_minT_12_sig-EQV-RMSND_geophy-bulkchem.dat

0 PassedModels_ModelA_Taylor_minT_15_sig-EQV-RMSND_geophy-bulkchem.dat
0 PassedModels_ModelA_Taylor_minT_1_sig-EQV-RMSND_geophy-bulkchem.dat
0 PassedModels_ModelA_Taylor_minT_20_sig-EQV-RMSND_geophy-bulkchem.dat
0 PassedModels_ModelA_Taylor_minT_25_sig-EQV-RMSND_geophy-bulkchem.dat
0 PassedModels_ModelA_Taylor_minT_2_sig-EQV-RMSND_geophy-bulkchem.dat
0 PassedModels_ModelA_Taylor_minT_3_sig-EQV-RMSND_geophy-bulkchem.dat
25175 PassedModels_ModelA_Taylor_minT_500_sig-EQV-RMSND_geophy-bulkchem.dat
0 PassedModels_ModelA_Taylor_minT_50_sig-EQV-RMSND_geophy-bulkchem.dat
0 PassedModels_ModelA_Taylor_minT_5_sig-EQV-RMSND_geophy-bulkchem.dat
0 PassedModels_ModelA_Taylor_minT_8_sig-EQV-RMSND_geophy-bulkchem.dat

Text S2.9 Comb-RMSND – CS

37533 PassedModels_ModelB_Orig_maxT_100000_sig-EQV-RMSND_geophy-bulkchem.dat
34287 PassedModels_ModelB_Orig_maxT_1000_sig-EQV-RMSND_geophy-bulkchem.dat
6361 PassedModels_ModelB_Orig_maxT_100_sig-EQV-RMSND_geophy-bulkchem.dat
239 PassedModels_ModelB_Orig_maxT_10_sig-EQV-RMSND_geophy-bulkchem.dat
414 PassedModels_ModelB_Orig_maxT_12_sig-EQV-RMSND_geophy-bulkchem.dat
735 PassedModels_ModelB_Orig_maxT_15_sig-EQV-RMSND_geophy-bulkchem.dat
0 PassedModels_ModelB_Orig_maxT_1_sig-EQV-RMSND_geophy-bulkchem.dat
1460 PassedModels_ModelB_Orig_maxT_20_sig-EQV-RMSND_geophy-bulkchem.dat
2185 PassedModels_ModelB_Orig_maxT_25_sig-EQV-RMSND_geophy-bulkchem.dat
0 PassedModels_ModelB_Orig_maxT_2_sig-EQV-RMSND_geophy-bulkchem.dat
0 PassedModels_ModelB_Orig_maxT_3_sig-EQV-RMSND_geophy-bulkchem.dat
19075 PassedModels_ModelB_Orig_maxT_500_sig-EQV-RMSND_geophy-bulkchem.dat
4379 PassedModels_ModelB_Orig_maxT_50_sig-EQV-RMSND_geophy-bulkchem.dat
16 PassedModels_ModelB_Orig_maxT_5_sig-EQV-RMSND_geophy-bulkchem.dat
115 PassedModels_ModelB_Orig_maxT_8_sig-EQV-RMSND_geophy-bulkchem.dat

42667 PassedModels_ModelB_Orig_meanT_100000_sig-EQV-RMSND_geophy-bulkchem.dat
39154 PassedModels_ModelB_Orig_meanT_1000_sig-EQV-RMSND_geophy-bulkchem.dat
7026 PassedModels_ModelB_Orig_meanT_100_sig-EQV-RMSND_geophy-bulkchem.dat
202 PassedModels_ModelB_Orig_meanT_10_sig-EQV-RMSND_geophy-bulkchem.dat
353 PassedModels_ModelB_Orig_meanT_12_sig-EQV-RMSND_geophy-bulkchem.dat
595 PassedModels_ModelB_Orig_meanT_15_sig-EQV-RMSND_geophy-bulkchem.dat
0 PassedModels_ModelB_Orig_meanT_1_sig-EQV-RMSND_geophy-bulkchem.dat
1010 PassedModels_ModelB_Orig_meanT_20_sig-EQV-RMSND_geophy-bulkchem.dat
1395 PassedModels_ModelB_Orig_meanT_25_sig-EQV-RMSND_geophy-bulkchem.dat
0 PassedModels_ModelB_Orig_meanT_2_sig-EQV-RMSND_geophy-bulkchem.dat

0 PassedModels_ModelB_Orig_meanT_3_sig-EQV-RMSND_geophy-bulkchem.dat
22336 PassedModels_ModelB_Orig_meanT_500_sig-EQV-RMSND_geophy-bulkchem.dat
2767 PassedModels_ModelB_Orig_meanT_50_sig-EQV-RMSND_geophy-bulkchem.dat
14 PassedModels_ModelB_Orig_meanT_5_sig-EQV-RMSND_geophy-bulkchem.dat
83 PassedModels_ModelB_Orig_meanT_8_sig-EQV-RMSND_geophy-bulkchem.dat

41189 PassedModels_ModelB_Orig_minT_100000_sig-EQV-RMSND_geophy-bulkchem.dat
37515 PassedModels_ModelB_Orig_minT_1000_sig-EQV-RMSND_geophy-bulkchem.dat
6071 PassedModels_ModelB_Orig_minT_100_sig-EQV-RMSND_geophy-bulkchem.dat
247 PassedModels_ModelB_Orig_minT_10_sig-EQV-RMSND_geophy-bulkchem.dat
442 PassedModels_ModelB_Orig_minT_12_sig-EQV-RMSND_geophy-bulkchem.dat
680 PassedModels_ModelB_Orig_minT_15_sig-EQV-RMSND_geophy-bulkchem.dat
0 PassedModels_ModelB_Orig_minT_1_sig-EQV-RMSND_geophy-bulkchem.dat
1139 PassedModels_ModelB_Orig_minT_20_sig-EQV-RMSND_geophy-bulkchem.dat
1586 PassedModels_ModelB_Orig_minT_25_sig-EQV-RMSND_geophy-bulkchem.dat
0 PassedModels_ModelB_Orig_minT_2_sig-EQV-RMSND_geophy-bulkchem.dat
0 PassedModels_ModelB_Orig_minT_3_sig-EQV-RMSND_geophy-bulkchem.dat
19325 PassedModels_ModelB_Orig_minT_500_sig-EQV-RMSND_geophy-bulkchem.dat
2883 PassedModels_ModelB_Orig_minT_50_sig-EQV-RMSND_geophy-bulkchem.dat
13 PassedModels_ModelB_Orig_minT_5_sig-EQV-RMSND_geophy-bulkchem.dat
164 PassedModels_ModelB_Orig_minT_8_sig-EQV-RMSND_geophy-bulkchem.dat